



*Facultad
de
Ciencias*

SIMULATION OF THE RESPONSE OF 3D PIXEL PARTICLE SENSORS UNDER MAGNETIC FIELDS

(Simulación de la respuesta de detectores de partículas pixelados 3D bajo la influencia de campos magnéticos)

Trabajo de Fin de Grado
para acceder al

GRADO EN FÍSICA

Autor: Cristian Quintana San Emeterio

Director: Jordi Duarte-Campderrós

Marzo - 2022

Abstract

The Large Hadron Collider (LHC) will undergo important upgrades in the coming years in order to increase its research capabilities. This will translate into a huge increase of the instantaneous luminosity and thus the radiation levels that the pixelated silicon sensors that form the inner layers of the experiments will have to cope with. An intensive R&D campaign of radiation-tolerant silicon sensors are currently underway in the main experiments of the LHC. The relatively new columnar pixel technology, known as 3D pixel detectors, is being considered because of their properties that make them inherently radiation resistant. Part of the development and characterization of this technology involves understanding its electrostatic properties in order to predict its response under the passage of ionizing particles. A common approach to accomplish this is performing electrostatic simulations to predict its transient response. Due to the complicated geometry and the relatively new use of this technology, there are almost no simulations available in the literature, therefore this work fills the gap on simulations of 3D pixel technology and its response as particle detector. The pixel response has been simulated for the 3D pixel cell configuration layouts being discussed at the Compact Muon Solenoid experiment, using the Ramo-Shockley theorem. The theorem allows to simulate the transient signals produced in the electronics by an ionizing particle through the electric and weighting fields of the sensor. A novel approach in both the calculations of both fields, based on a relaxational method for the weighting field, and on the use of an equivalent charge distribution instead of solving the Poisson equation for the electric field, allow to simplify the algorithms and therefore the computation times, providing good qualitative and quantitative results. Finally, the simulation is used for the first time to simulate and understand the transient signals of this 3D pixels under the influence of magnetic fields, such as those in the LHC experiment.

Keywords: particle detectors, radiation damage, 3D pixelated silicon sensors, transient current response simulation

Resumen

El Gran Colisionador de Hadrones (LHC por sus siglas en inglés) experimentará en los próximos años importantes mejoras que aumentarán su capacidad de investigación. Esto se verá traducido en un enorme aumento de la luminosidad instantánea y, por tanto, un incremento sin parangón de los niveles de radiación que tendrán que soportar los detectores tipo pixel de silicio, los cuales se encuentran en las capas más profundas de los experimentos. Actualmente existe una campaña intensiva de I+D para obtener sensores de silicio resistentes a la radiación, que está siendo llevada a cabo por los principales experimentos del LHC. La relativamente nueva tecnología de píxeles columnares, conocida como detectores de píxeles 3D está demostrando ser inherentemente resistente a la radiación. La caracterización de este tipo de detectores comienza con la comprensión de sus propiedades electroestáticas, necesaria para predecir su respuesta al paso de partículas ionizantes. El primer enfoque común que se suele realizar es generar simulaciones electroestáticas y así obtener las respuestas transitorias. Debido a que estos detectores están actualmetne siendo estudiados y también a la complejidad de su geometría, casi no existen simulaciones disponibles en la literatura. Este trabajo ampliará el conocimiento existente en cuestión de simulaciones de tecnología de píxeles 3D y su respuesta como detector de partículas. Se ha simulado la respuesta que se obtendría de dos tipos de diseño de pixel 3D que actualmetne están bajo discusión en el experimento CMS. Las simulaciones se han realizado utilizando el teorema de Ramo-Shockley, theorema que permite simular señales transitorias inducidas en la electrónica cuando una partícula ionizante atraviesa el sensor. La simulación requiere por tanto del cálculo de los campos de pesado y campo eléctrico electrostático, los cuales se han obtenido desde un enfoque novedoso. Mientras que el campo de pesado se ha obtenido a través de un proceso iterativo utilizando un método de relajación; el cálculo del campo eléctrico se ha resuelto a través de una aproximación de distribuciones de carga puntuales. Este método alternativo de resolver la ecuación de Poisson permiten simplificar los algoritmos y por tanto los tiempos de cálculo, proporcionando buenos resultados cualitativos y cuantitativos. Por último, la simulación se utiliza por primera vez para simular y comprender las señales transitorias de estos píxeles 3D bajo la influencia de campos magnéticos, como los que tendrán que soportar en los experimentos del LHC.

Palabras clave: detectores de partículas, daño por radiación, sensores de píxeles 3D, simulación de señales transitorias de corriente

ACKNOWLEDGEMENTS

(Agradecimientos)

Quisiera empezar agradeciendo a Jordi toda la paciencia y entrega que me ha brindado. Desde que me ofreció la posibilidad de realizar este trabajo no ha cejado en su empeño por formarme en una nueva disciplina que, sin ninguna duda, ha superado completamente con creces mis expectativas. Gracias a ello puedo decir que el recuerdo de los buenos ratos que hemos pasado y las aptitudes que he desarrollado me acompañarán a donde quiera que vaya.

Dar las gracias también a la gente que ha dedicado parte de su tiempo a ayudarme a hacer crecer este proyecto. Especialmente a Salvador, Óscar y Giulio del Institut de Microelectrònica de Barcelona por compartir sus conocimientos conmigo, así como a Ernesto, mi antiguo profesor de Electromagnetismo, al que también acudí. A Julio también, que se ha preocupado y me ha aconsejado en las labores más administrativas.

Por último me gustaría que se valorase la labor de la gente que forman la Universidad de Cantabria y del Instituto de Física de Cantabria, los cuales no sólo me han proporcionado los conocimientos de los que presumo, sino que también se han convertido en una parte importante de mí.

Contents

1. Introduction	7
1.1. The Compact Muon experiment	7
1.2. High spatial resolution particle detectors	8
2. Fundamentals of Silicon Detectors	13
2.1. Silicon properties	13
2.2. The P-N junction.	15
2.3. Detector-radiation interaction	16
2.4. Signal generation	16
3. Methodology	19
3.1. Fields' calculations	19
3.2. Simulation methodology	22
4. Analysis and Results	25
4.1. Doping profiles	25
4.2. Electric field.	26
4.3. Transient signals.	32
5. Conclusions.	46
A. Extra figures	50

Chapter 1

Introduction

This chapter introduces the context of this work, i.e., silicon detectors used in elementary particle physics experiments. The Compact Muon Solenoid experiment, an experiment of the Large Hadron Collider, is functionally described, and in particular the role of pixelated silicon sensor as high spatial resolution particle detectors. The columnar pixel sensor technology is presented, discussing its advantages and drawbacks, and a bibliographic search shows the lack of studies on the simulation response of this technology, justifying the scope of this work.

1.1. The Compact Muon experiment

The Large Hadron Collider (LHC) at CERN (Geneva area, Switzerland), is the largest particle accelerator in the world with a total length of 27 km. Particles, usually protons, are accelerated in the collider ring up to energies near 7 TeV making this accelerator also the most powerful. They collide in four different points (see figure 1.1) of the ring where dedicated experiments are placed to measure the debris of the collisions in order to reconstruct and infer the processes produced when the particles hit at 14 TeV in its center of mass.

The Compact Moun Solenoid [2] (CMS) is one of these experiments. As its name suggests, CMS is built around a large solenoid magnet, with a cylindrical geometry surrounding the interaction point where protons collide. The experiment has been built to be compact and hermetic in order to maximize the detection volume. Each particle collision creates large-mass unstable particles that rapidly decay into stable particles that CMS can detect. Those stable particles travel throughout the experiment, from very close the point of the collision until they are absorbed or escape, passing through different layers of detectors that allow their momenta, energy, charge and type of particle to be measured. With this information, the collision can be reconstructed and further analyzed.

The experiment is constructed as a cylindrical onion, with specific layers of components specialized in detecting different particle properties as it can be shown in figure 1.2. The outermost component layer is composed of muon detectors, since muons are the only particles will be able to reach them, as they can transverse all the others components of CMS without almost interacting. The momentum, energy and charge of the muons can be measured with those muon chambers. The next inner layers are the hadronic and electromagnetic calorimeters. They detect hadrons (like neutrons, protons, pions and kaons) and electrons, positrons and photons respectively by measuring the energy that they deposit

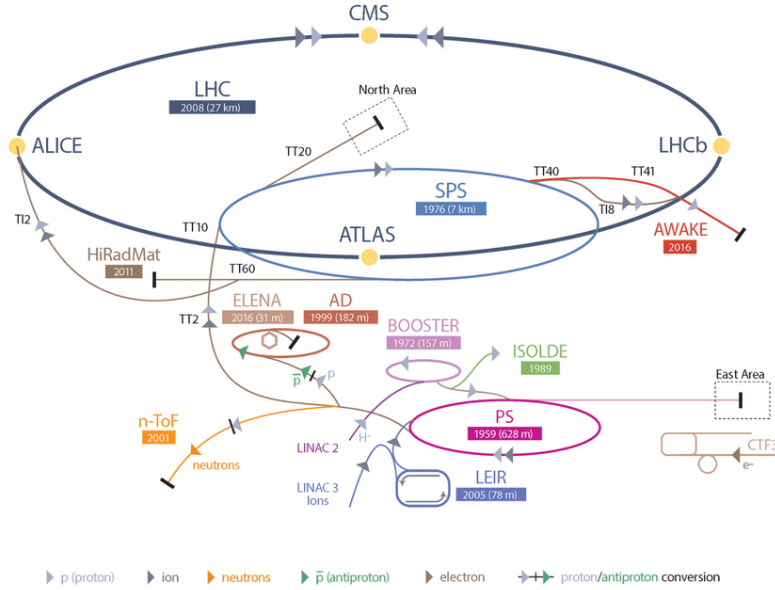


Figure 1.1: The full accelerating chain at CERN, where the LHC is the last and largest element. The four collision points, where the experiments are built, are identified as yellow points. Figure extracted from [1].

in dense materials such as brass, steel or tungstate crystals. The measurement process is destructive and the measured particles are absorbed by the material. The innermost components of CMS are two structures based on silicon detectors: the tracker and the pixel vertex detector. Both sub-detectors, provide a very high spatial resolution [3], able to reconstruct the trajectories (called *tracks*) of the particles. The superior resolution of the vertex sub-detector allows to identify the decay of particles, i.e., the point where two or more tracks come from, which is called *vertex*. This accuracy is accomplished with pixelated silicon sensors acting as particle detectors, capable to identify that a charged particle is passing by with little or no disturbance of the particle trajectory and energy. The magnetic field is used to curve the trajectories of the charged particles while they transverse the tracker in order to measure their momentum (through curvature) and their charge. Being the tracker, in particular the vertex detector, very close to the beam pipe, it will be the component that will have to cope with the highest levels of radiation. The detection technology used to build the tracker, which is silicon, has to be radiation tolerant.

1.2. High spatial resolution particle detectors

Silicon sensors acting as particle detectors work in a similar way than a drift chamber [5]. A drift chamber consists in a closed region filled with a gas acting as sensitive medium, and two electrodes creating an electric field inside the region. When an ionizing particle cross the detector, it interacts with the neutral atoms of the gas, ionizing them and creating two charge particles per atom: the ejected electron and the positive ion. Those charge carries will be drifted away due to the presence of the electric field, inducing an electric signal on the electrodes, and therefore "detecting" the impinging particle.

Silicon sensors are solid state equivalents to the drift chamber, with better performance

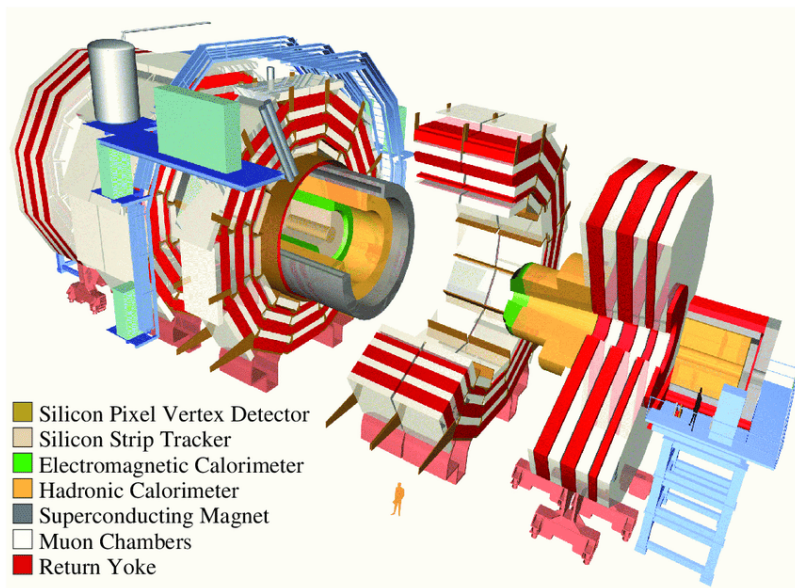


Figure 1.2: The CMS detector opened to allow the visualization of its internal structure. The different sub-detectors and components are identified with different colors. Figure extracted from [4].

and less particle interaction (due to its lower ionization energies). However, some manipulations are needed in the silicon to be used as particle detector, such as doping the silicon with impurities and create a structure with different combinations of doped regions (this will be explained in more details in section 2). As in drift chambers, silicon sensors are composed by a sensitive medium (called bulk) where radiation can interact and produce charge carriers. Those charge carriers are drifted by the internal electric field, producing a signal that indicates that a particle has been detected. The electric field is generated by the union between the bulk and the highly doped areas (P-N junction). Figure 1.3 shows a typical silicon detector with planar geometry, where it can be seen all the elements previously described.

In planar sensors, the bulk thickness determines the maximum amount of charge carriers that the incoming particle can generate. Thickness is also the dimension that determines the distance the charge carriers have to travel before being collected on the electrodes, since the electric field lines are orientated in that direction. Therefore, increasing the amount of charge for a given particle implies increasing the drift distance. This coupling has implications when trying to create radiation tolerant devices. Under real working conditions silicon devices experiment two types of radiation: the particles that generates signal and non-ionizing radiation also interacts with the silicon and generates defects on the crystal lattice. The damage produced acts like charge carriers traps, capturing charge carriers in their way to the electrodes, and thus decreasing the recollected charge. In order to mitigate the charge losses, the sensor bulk can be increased, but at the same time the probability to trap carriers will increase as well. Therefore, there must be a trade-off between trapping probability and charge generation, so increasing the thickness can not fully mitigate the radiation damage effects.

For the LHC upgrade (called High-Luminosity LHC), the accelerator will be able to

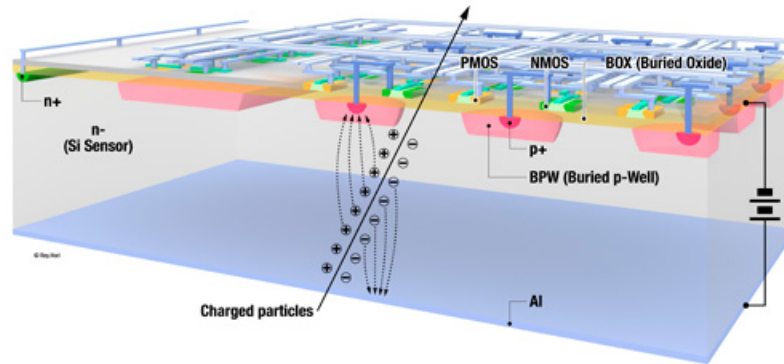


Figure 1.3: Schematic view of a planar silicon detector. The bulk region is represented in light gray, and the highly doped areas in pink are used to create the P-N junctions, responsible for the generation of the internal electric field. The figure also shows the charges carriers generated by an ionizing particle, and their drift under the electric field. In this example, the sensor bulk is composed of n-type impurities, while highly-doped p-type regions are inserted into it to create the P-N junctions. Figure obtained from [6].

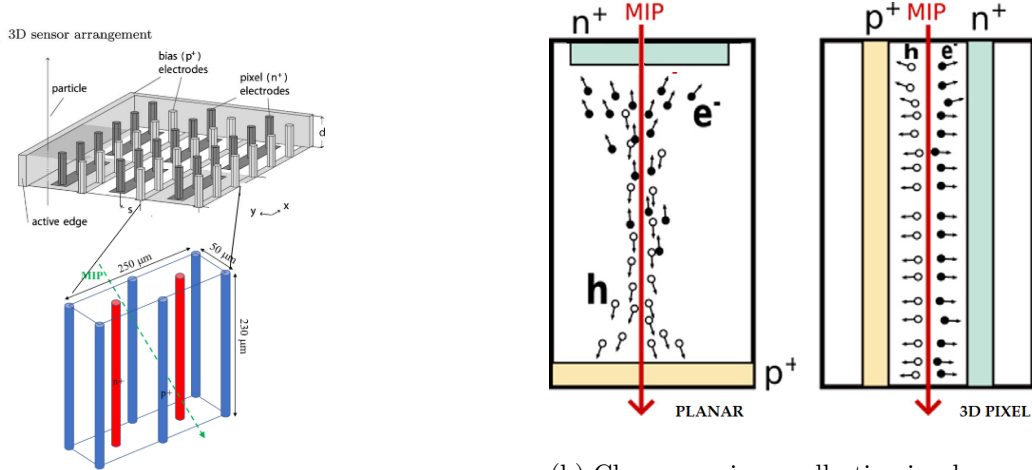
reach very high luminosity¹ levels during the data taking [8]. The innermost part of CMS will have to cope with an unprecedented radiation levels, therefore new approaches and technologies have been explored during the R&D campaign. Columnar pixel detectors [9] are a relatively new proposed technology with some properties made them intrinsically radiation resistant.

As it is shown in figure 1.4a, 3D pixel detectors are based on a different architecture than the usual planar detectors. The P-N junctions are created by growing columnar highly-doped silicon inside the bulk, on contrast to the planar sensors where the the highly-doped silicon is grown on the bulk surface, as figure 1.4b is representing. This differences have a deep impact in the sensor performance after irradiated as the 3D sensors decouples the amount of charge created by an ionizing particle, i.e., the thickness of the bulk, from the distance the charge carriers have to travel before being collected. In the case of the 3D pixels, the thickness of the sensors can be increased to create enough charge after irradiation, while keeping a short drift distance, as the the electric field lines are perpendicular to the thickness dimension. The columnar design is thus inherently radiation resistant, as irradiation-induced damage can be minimized by reducing the charge carrier drift distance and increasing the electric field near the electrodes [8]. On the contrary, in planar detectors both things can be achieved by making thinner diodes, but consequently, the collected charge is reduced.

However, there are some drawbacks on the columnar geometry. The 3D pixels sensors suffer of non-homogeneous electric fields along the pixel volume and with certain regions of zero field, which translates in different responses depending on the region through which the

¹Number of particles delivered per volume and time unit. It have a direct relation with the collision rate and by extension with the radiation levels [7].

particle passes. It also introduces regions of inefficiency, since the highly doped columns are occupying a sensitive area. As a side effect, the simulation of the response becomes more difficult to predict than in planar detectors, as it is needed to resolve a three-dimensional second order differential equations (Poisson and Laplace for the electrostatic and weighting fields respectively), while in the case of the planar sensors, the problem can be simplified to one dimension.



(a) The bottom figure shows two pixel cells from the matrix (top). The charge is collected in each N-P junction (red), limiting the ohmic columns (blue) the pixel volume. Figure extracted from [10]

(b) Charge carrier recollection in planar and 3D sensors (right), showing the decoupling on the 3D sensors between the amount of charge an incident particle can create (thickness direction) and the charge carrier collecting distance. Figure provided at [11]

Figure 1.4: Columnar pixel technology compared with planar.

1.2.1. Simulation on 3D pixels. State-of-the-art.

The simulation of the response of a particle detector allows the study as well as the optimization of (new) structures without having to actually manufacture them, and therefore saving an enormous amount of money and time. Simulation are an essential ingredient of any current research, specially in the elementary particle physics field.

Within the field of the semiconductor detectors structures, the main tool used to develop and optimize silicon devices and technologies are the Computer-Aided Design (TCAD). Programs based on *Sentaurus* [12] are widely used to simulate and understand the electrostatic behaviour of 2D and 3D devices. *Sentaurus* has been applied to 3D pixel sensor structures, like it can be seen in fig. 1.5. This software performs the simulation defining a volume with the device under study. This volume is converted into a mesh of points (finite elements) to solve the differential equations (Poisson, continuity, ...) numerically. This algorithm needs a large number of finite elements to provide sensitive results, and therefore the computation times used to be unmanageably large.

There are other tools with similar purposes, but with different approaches, trying to be faster even at the cost of losing some accuracy in the results, as they are not calculating precisely the full set of differential equations to obtain the sensor response. For example, *Garfield++* is a software that traditionally has been used to simulate the particle interactions with gases, but also can be used for semiconductors [13]. *Allpix²* is another

generic simulation framework developed at CERN collaboration but more oriented to pixel detectors [14]. It is able to inject independent TCAD simulations. An interesting feature that this program gives is a support to introduce the effects of magnetic fields, translating it to Lorentz charge drifts.

IFCA has also developed a tool called *TRACS*, incorporating an element finite solver, to obtain simulations of signals generated on semiconductors being based on the Ramo-Shockley theorem (see section 1.2.5) assuming several approximations [15].

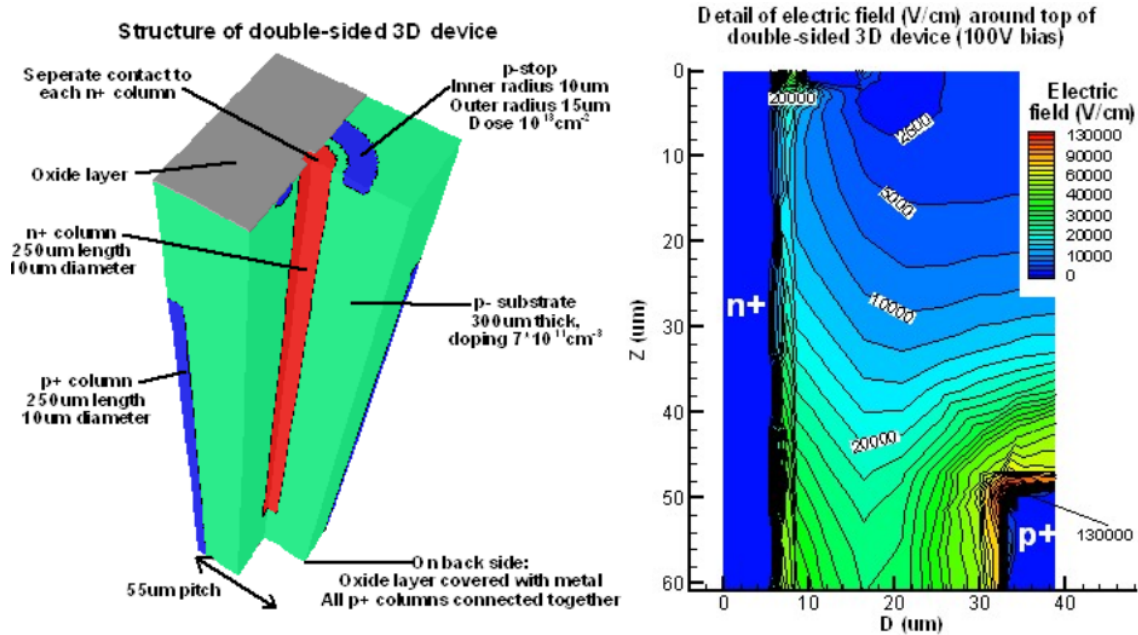


Figure 1.5: Example of one 3D pixel sensor simulation of a double-side 3D pixel sensor using a TCAD simulation [12]. The left figure shows the doping profiles used to solved the electric field inside the bulk, shown on the right figure.

Despite the range of tools and software available, there are hardly any simulations of 3D technology in the literature. Most simulations are made during R&D optimization and fabrication process by the foundries but kept private. The main goal of this end-of-degree project is to obtain a simulation optimized to predict the behaviour of the 3D pixel sensors, and able to be used in different working scenarios, including test beam characterization campaigns and under magnetic fields. The tool could be very useful, once validated with experimental data, to understand the complicated electrostatic patterns of the internal electric field, and therefore its induced signal when a particle pass through.

Chapter 2

Fundamentals of Silicon Detectors

A brief introduction into the fundamental physics needed to understand and justify the simulation of the response of the novel 3D pixel detectors is provided in this chapter. Specifically, the Ramo-Shockley theorem is introduced to understand the different components to be calculated if one wants to simulate the electrical signal that appears in a 3D silicon sensor when an ionized particle passes through the detector.

2.1. Silicon properties

Silicon is the semiconductor most widely used in electronic applications and is responsible for the technological development of our days. It is part of most of the electronic devices because its electrical and mechanical properties, making it also an excellent material for the construction of solid state particle detectors.

With 14 electrons, has a configuration $[\text{Ne}]3s^23p^2$ (equivalent to carbon) so the crystal structure is the well known diamond-like face-centered cubic. Since the number of valence electrons and the number of electrons to fill external shell is in both cases four, the formation of sp^3 orbital hybridization (tetrahedral geometry) is feasible.

By promoting an electron from the valence band to the conduction band¹, it leaves behind a vacant state in the valence band that another electron can occupy. This vacant is called *hole*, and from the electric point of view acts as a pseudo-particle under the presence of an electric field. So, whenever an electron occupying a crystal lattice valence band is ionized, by an external particle for instance, the result will always be an electron-hole pair (e^- - h^+) which behave as quasi-free particles, and drift as negative and positive charges respectively (*charges carriers*) if an electric field is applied. The main difference between electron and holes is that moving a hole in the lattice requires the coordination of bounded electrons moving between the outermost atomic shells, so the mobility of holes is about three times lower than the electron mobility, which on the contrary follows a ballistic movement [16].

Eventually, the opposite process happens when both elements recombine. It should take about a few seconds on average, but natural impurities in the crystal introduce levels in the middle of the gap making this time reduced by a 10^6 - 10^9 factor. Those impurities can also act like traps kidnapping temporally e^- or h^+ .

The energy gap assures an almost negligible noise level for common applications at room temperature where the thermal energy at room temperature is about 25.9 meV [17].

¹The energy gap between valence and conduction bands is about 1.12eV at room temperature.

If one wants to use the silicon as a particle detector, despite the number of electrons that can jump to higher bands is very low (only one atom in 10^{12} is ionized (at 300k) [16]), this number is still ridiculously huge if we compare it with the number of e^-h^+ that are generated by and ionizing particle. Another problem present in order to use silicon as particle detector is that silicon behaves almost like an insulator. That is why it is necessary adding impurities (doping) to create extra energy levels and therefore increase the number of charge carriers, enhancing the conductivity.

If the silicon is doped with atoms from the 15 group (phosphorus, arsenic, antimony) the lattice structure will not change. As they are V type elements, the neighbour silicons can only bond with four of these electrons, so it remains one energetically favoured to unbound the atomic system, injecting electrons in the conduction band but no holes. This kind of dopant is called *donor* (donate an electron) and the region is called n-type, as there are a majority of negative charge carriers. Silicon can also be doped in the same way with 13 group elements (III type: boron, gallium, indium). In that case, as this impurities has 3 electrons in the outermost shell, one of the electrons of the four silicon atoms closest to the impurity is unpaired, creating a hole without creating an electron in the conduction band. In that case, the impurities are called *acceptors*, and the region p-type, as the majority of the charge carrier population are positive charge carriers (holes). Figure 2.1 shows a simplified representation of doping a silicon lattice crystal. This break in the e^-h^+ equivalent distribution is the reason behind the diffusion processes and the generation of electric fields inside complex semiconductor devices, where different doped materials are combined. As an essential consequence, introducing impurities will create an asymmetry between the charge carrier populations.

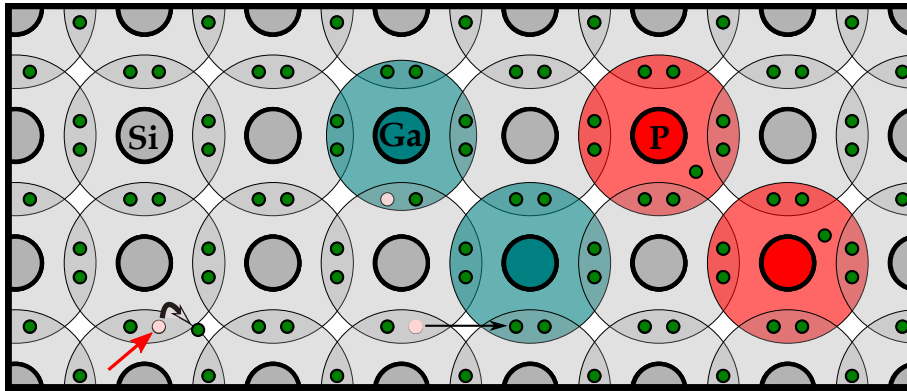


Figure 2.1: Scheme of a silicon lattice doped with impurities of both types, n and p. In this example gallium and phosphorus are represented. Silicon atoms share their four electrons to form the lattice. If we introduce a phosphorus impurity we obtain a quasi-free electron, electron that do not contributes to any bond. If gallium is added the situation is the opposite. Gallium do not provides enough electrons tho form the four bonds. This electron lack is known as a hole. Quasi-free electrons and holes can also be generated when an external or internal process ionizes one of the silicons (red arrow).

2.2. The P-N junction.

The importance of the semiconductors lies on the possibility to combine n- and p-type doped regions to make hetero-structures, which electrical properties depend on the selection of the materials, doping impurities and doping levels. The resulting device is the well known diode.

Diodes' electrical behaviour is defined by the junction between the two dopant regions, and it is called "the P-N junction". First of all it is need to say that the semiconductor have not a global excess of charge, the excess of free carriers refers to the unpaired electrons in both materials. The excess of electrons and holes diffuses when the union is formed, and they recombine as soon as they entered into the other regions. This process leaves behind ions fixed in the crystal lattice, and while the electron and holes are recombining and removing the region close to the metallurgical junction of charge carriers, those ions creates an electric field that opposites the diffusion of the charges. At certain point the system reaches an equilibrium where a region free of charge carriers, the depletion zone, is created. The process is explained in 2.2.

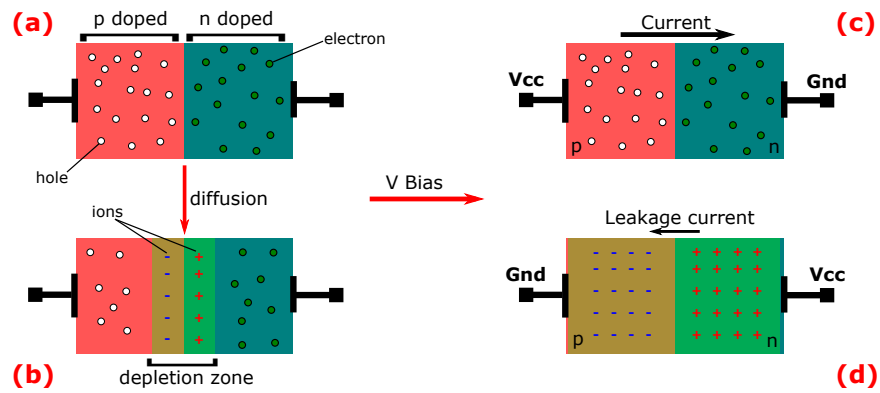


Figure 2.2: Simplified explanation of the creation of the depleted region in a P-N junction: (a): device right after the union, before the charge diffusion; (b): built-in depletion region emerging as consequence of diffusion and the electric field; (c): Diode in direct polarization, the voltage difference can create a current without a significant resistance; (d): Diode in reverse polarization, the depletion zone extends over the whole device (Detector mode).

As we can see in figure 2.2-c, if we apply a bias voltage V_{Bias} with that specific polarization the device allows the charge flow because there is no depletion zone. Nevertheless, we have to surpass the intrinsic electric potential of 1V approx if we want the diode operation. The effect is the opposite if we reverse the polarization (2.2-d), expanding the depletion zone up to V_{Bias} is so high that depletes all the charge carriers. At this limit V_{Bias} is equal to the so-called depletion voltage V_{dep} . In that condition, the maximum sensitive volume is available to detect any impinging particle. Moreover, inside the sensor the electric field present, will drift any charge generated in the depleted region, allowing to measured it. Therefore, the device is a particle detector. Increasing V_{Bias} above V_{dep} contributes to increase the electric field which means less drifting time, although but also increases the leakage current.

2.3. Detector-radiation interaction

Incoming particles that cross the detector can produce signal if they have the capacity to ionize the medium: this depends on the energy that the particle can deposit and the fact the particle is charged or neutral. Different particles will produce different signals due the differences in the interactions. For heavy particles the process is well defined by the Bethe-Bloch formula, which gives information about the energy loss of a particle in a specific amount of material. For lighter particles such as electrons, with a mass equal to the scattered particles, the formula needs to introduce some modifications, as well as include other forms of interaction such as bremsstrahlung.

Figures 2.3 shows the interaction of two different detector devices, measuring different kind of particles. Both figures show regions where the energy of its matter interaction minimum. Those particles whose regime of energy are in their minimum are called Minimum Ionizing Particles (MIPs). MIPs a similar signal independent of what particle is. When passing through a thin detector (100-500 μm for typical High-Energy detectors), produce about 80 e-h pairs per μm in a process that needs in average 3.6 eV for each pair created [17].

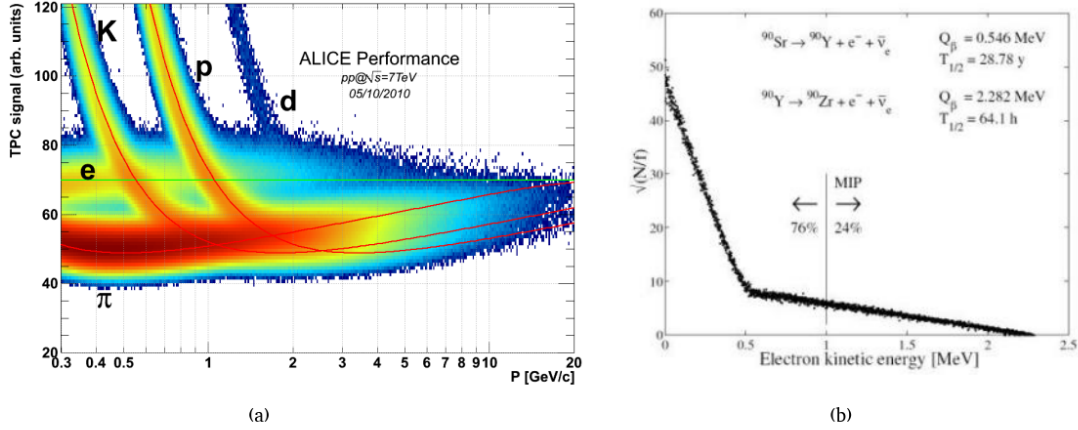


Figure 2.3: According to the Bethe-Bloch equation, the loses by ionization that a particle experiments when it cross a medium has a minimum that depends of the momentum of the particle. The particles with that momentum are called minimum ionizing particles (MIPs). The two charts in the figure are obtain from real experiments. It can be seen that the fitted data presents a behaviour according the Bethe-Block theory. Images taken from: [18][19]

2.4. Signal generation

In silicon-based detectors, the interaction between the high-energy particles and the semiconductor bulk generates e-h pairs. These charges establish also a charge distribution in the electrodes through an electric field. For example, in the case of a charge q at a distance z_0 of a 2D electrode with coordinates (x, y) , generates an electric field $E=E_z$ ($E_x = E_y = 0$) as follows [20]:

$$E_z(x, y) = \frac{-qz_0}{2\pi\epsilon_0(x^2 + y^2 + z^2)^{\frac{3}{2}}} \quad (2.1)$$

And interesting feature of this process is that the induced charge Q_I is equal to q , and the drive of q (at a velocity $v = v_z$ for example) causes a variation of Q_I as function of time, that is to say a current I [21]:

$$Q_I = \epsilon_0 \iint_S E_z(x, y) dx dy = -q \quad (2.2)$$

$$I(t) = -\frac{dQ_I}{dt} = -\frac{\partial Q_I}{\partial z} \frac{dz}{dt} \quad (2.3)$$

The simplicity of the 2D sensors make possible to obtain analytic solutions of the current generation, but for more complex setups it is recommendable to appeal the Ramo-Shockley Theorem.

2.4.1. The Ramo-Shockley Theorem.

The Ramo-Shockley Theorem (RST) allows to determine the induced current in an electrode i by the charge q in its proximity [22][23]. This theorem is a shortcut, a mathematical construct but it can be seen that it is derived from the principle of energy conservation. It uses a fictitious field, the weighting field Ψ to evaluate the influence of the geometry of the electrodes with the movement of the charges.

The RST is valid under the following conditions or approximations. The first is a quasi steady state approximation: the variation of the fields involved is considerably higher than the movement of the charges, so it can be assumed that $\partial B, D/\partial t = 0$. This fact is very important because allows to separate the problem in a linear contribution of the fields. The second condition is the situation of equilibrium in the electric field inside the detector (charge distribution fixed) so the transitory effects or powering up the device are not included. At this point, the problem to be resolved is:

$$\nabla^2 \phi(\vec{x}) = -[\rho(\vec{x}) + q\delta(\vec{x} - \vec{x}_0)]/\epsilon \quad (2.4)$$

As every electrode and charge can be approached separately, the solution goes through the superposition principle, and using Green's Theorem we resolve that the induced current $I_{q,i}$ by the charge q in the electrode i is :

$$I_{q,i} = q\vec{E}_{\Psi_i} \cdot \vec{v}_q = q\nabla\Psi_i \cdot \mu_q\vec{E}_{pixel} \quad (2.5)$$

where $\vec{E}_{\Psi_i} = \nabla\Psi_i$ is the weighting field derived from its potential, \vec{v}_q is the velocity of q and is related proportionately with the pixel's electric field \vec{E}_{pixel} via the mobility μ of q .

Thus, the RST allow us to calculate the induced charge on the electrodes given by a moving charge carrier inside the pixel bulk by knowing the electric field in our detector (which will give the velocity or trajectory of the particles), and the weighting field. The latter element can be calculated removing all charge sources, and setting the electrode of interest at 1V of potential and the rest of electrodes grounded (0V); and solving the Laplace's equation $\nabla^2\Psi_i = 0$ with those boundary conditions. The electric field inside the bulk, cause of the charge carriers drift, can be calculated by solving the Poisson' equation where the source charge distribution is produced by the dopant profiles, $\nabla^2\phi = \rho/\epsilon$.

2.4.2. Transient signal under magnetic field.

Equation 2.5 can be modified to introduce a magnetic field \vec{B} immersed in the detection volume. Because we have two types of charge carriers being drifted (e-h), these will experience the Lorentz force differently:

$$\vec{F}_q = q(\vec{E} + \vec{v}_q \times \vec{B}) = q(\vec{E} + \mu_q \vec{E}_q \times \vec{B}) \quad (2.6)$$

Note that this equation is valid for charges travelling through a at constant speed. The force term in eq.2.5 can be identified and replaced it by the force that includes magnetic effects:

$$I_{q,i} = \nabla \Psi_i \cdot \mu_q q \vec{E}_{pixel} = \nabla \Psi_i \cdot \mu_q \vec{F}_q \xrightarrow{\vec{B}} I_{q,i} = \nabla \Psi_i \cdot \mu_q q (\vec{E} + \mu_q \vec{E}_q \times \vec{B}) \quad (2.7)$$

Chapter 3

Methodology

The methodology followed to create the simulation is exposed in this chapter. The calculation methods used to obtain the Ramo-Shockley theorem ingredients, such the electric, and weighting fields, are detailed and discussed. We described the relaxational method to calculate the weighting potential in order to solve the Laplace equation; the charge distribution method used to compute the electric field; and finally a modified version of the Ramo-Shockley theorem to deal with magnetic fields. The resources that were used and the general simulation process are also explained.

3.1. Fields' calculations

3.1.1. The weighting field: relaxational method

This method is often used to solve elliptic partial differential equations in a 3D space $p(x_1, x_2, x_3) = p(x, y, z)$ using an iterative technique [24]. Our particular problem tries to solve the Laplace equation at each point of the pixel cell and around it.

$$\nabla^2\Psi = 0 \tag{3.1}$$

Iterative methods do not deal with the full calculation of the field at once (see eq. 3.1). Instead, the full volume is homogeneously discretized to a certain number of points (denoted by the suffix i) and the problem can be focused on each one, $\nabla^2\Psi_i = 0$. Using a Taylor expansion of Ψ_i we can make an approximation of the second order derivatives and express the desired relation as:

$$\nabla^2\Psi_i = 0 = \sum_{d=1}^3 \frac{\partial^2\Psi_i}{\partial x_d^2} \implies \Psi_i(p) = \frac{1}{6} \sum_{e=1}^6 \Psi_i(p_{ne}) = 0 \tag{3.2}$$

Equation 3.2 establish a relation between the potential at a given point of interest p and its six first neighbour points " p_{ne} " (3D geometry). This means that when the field is properly solved, the potential at each point is equal to the sum of the potentials of the closest points divided by a six factor.

At this point the problem is easy to solve as long as the pertinent boundary conditions (b.c.) are taking into account. Only three boundary conditions are applied since we do not consider a system out of equilibrium. Two of them, Dirichlet's b.c. and Neumann's b.c. are imposed by the method. The third kind derives from the geometry of the problem as symmetric b.c.s.

Dirichlet's boundary condition fix the potential of the collector electrode (where the charge is induced) at 1V and the rest are grounded [23] (0V). We will consider 1 central pixel, plus several neighbour pixel cells, therefore all n- and p-columns of the neighbour pixels as well as the back-end are grounded.

The transitions between the surface of the detector and the air modify the field. The second b.c.s (Neumann) has to be included because the field in the surface of a conductor in equilibrium only can be oriented in one direction. Specifically, the field lines have to be perpendicular to the limiting surfaces S_L and thus fixes the relation of the first derivatives of the potential: $\nabla\Psi_i(p(S_L)) \parallel n_{S_L}^{\vec{}}$. The easiest way to implement that is to impose a value V for the surface points equal to the closest points in the normal directions.

Symmetry conditions are the last type of b.c. The pixel matrix (for both configurations) has at least a 4C symmetry, so in order to reduce the simulation times only one quadrant centered in our electrode i have to be computed. It means that the points adjacent to the symmetry planes have the same potential value.

The iterative method starts by fixing the b.c.s and setting an initial value for those points corresponding to the bulk space. The chosen value was zero for our simulation because it is easier to see the progress of the running program. Then is when we analyze the deviation of the assigned potential of each point with the theoretical value that should have in relation with the potential of the closest points (eq.3.2). This difference (absolute value) is called residual or rest R (see eq.3.3).

$$R(p) = \left| \Psi_i(p) - \frac{1}{6} \sum_{e=1}^6 \Psi_i(p_{ne}) \right| \quad (3.3)$$

The relaxational method tries to reduce the residuals by modifying the potential of the point with the largest residual: at each iteration the maximum residual is found, the potential corresponding to the same point is changed to fit the theoretical value and finally the residuals are recalculated according to the new value. This procedure reduces gradually the rests until the largest R is below a desired tolerance, which represents the maximum error with the real field.

The discretized volume should include not only the central pixel but a matrix of them. This decision has to be taken by looking the geometry of the pixels, and specially the relative distance between the central pixel and the electrodes in the closest cells. The influence of external electrodes could dominate the behaviour of the potential at certain points of the detector. This volume should also be extended to let the potential "relax" and even further if we want to analyze the induction process in other pixels by the charge that is collected in other regions.

3.1.2. The electric field: point charge distribution method

The resolution of the electrostatic problem given by a charge distribution source, i.e. the Poisson equation, is solved usually by numerically finite elements methods, like TDAC-based software. The method used in this work avoids resolving the Poisson's equation in the pixel cell by using a different approach.

We start with the initial approximation of total ionization, meaning that all the impurities are ionized. The impurity ions are the sources of the electric field, and we can obtain the charge distribution directly from doping profiles. Instead of working with a continuous charge distribution, we need to discretize the total volume. As if they were point

charges, each point is attributed a total charge according to the doping profile and the volume it represents. This would be the equivalent of translating a microscopic effect to a larger scale. If we treat these quanta as sources of electric field, we can use the Coulomb's equation to solve for the total field. The total field would be, instead of the integral over the entire volume of the effect of the continuous charge distribution, the summation of the effect of the quanta. The discretization of the continuous charge distribution needs to be made carefully because this transition introduces an effect that tends to overestimate or underestimate the real potential. Passing from a quasi-continuous to a discrete formulation by means of a correction function is needed.

The introduction of a $f_s(r)$ as the correction function solves this geometrical artifact, a function approaching to one at infinity and to 0 when the distance is $r = 0$. This function is just an activation function that slows down the discrete step (instead of a Heaviside step, which would adapt pure discrete distances). Sigmoid functions are good candidates as they shown the wanted behaviour. We have used the function $f_s(r) = [1 - e^{-ar^b}]$, where r is the distance between the point that we are evaluating and the charge, and a and b are parameters to be fitted. The electric field inside the cell in this charge approximation will be

$$\vec{E}(p) = \int_V \frac{K_r \rho dV}{r^2} \vec{u}_r \approx \sum_i^N f_s(r) \frac{K_r q_i}{r^2} \vec{u}_r, \quad (3.4)$$

being p the point where the field is being evaluated, K_r the electric constant relative to the medium, and ρ is the charge density distribution. Thus, $f_s(r)$ can only be omitted when the simulated contribution to the electric field it is done at enough distance of the charge distribution.

In order to perform a faster simulation, it is found that working with the potential field instead of the electric field is preferable. As the potential is a scalar, calculating the potential instead only requires one calculation per point, in contrast with the 3-dimensional electric vector field. This will reduce the amount of computations that need to be performed. Furthermore, calculating the potential attenuates the geometrical effects making $f_s(r)$ less relevant. This is because the electric field has a quadratic relation with the distance factor (r), which introduces the geometrical artifacts also with an exponent. The potential is then defined as:

$$V(p) = \int_V \frac{K_r \rho dV}{r} \approx \sum_i^N f_s(r) \frac{K_r q_i}{r_{p,i}} \quad (3.5)$$

In order to avoid the geometric artifacts it is needed to adjust the sigmoid function to our discretization. A charge distribution with a known analytical expressions for the electric potential and electric field can be used in order to compare and gauge the effect of the approximations with an exact analytical solution.

The sigmoid function was adjusted to an uniform spherical charge distribution and studied different scenarios. Figure 3.1 shows the main artifacts that appear when the sigmoid function is not introduced. The method of computing first the potential and then the electric field introduce artifacts when the continuity of the fields experiment an abrupt change. The artifact with largest effect is due to the discontinuity of medium. The points per unit of measurement (*ppum*) indicates the grade of discretization that is introduced. In our case we have chosen 1 point/ μm in each dimension. Under this discretization the geometry effects are not very important. It can be noted in figure 3.1 that the behaviour

of the charge distribution method works well, when no abrupt transitions happen. The discrepancy between the real and the simulated fields is below the 8 % in the worst-case scenario. As we do not have fast transitions and we compute the electric potential, we can avoid finally using the correction function assuming that error. The doping profiles are not abrupt since during detector fabrication the charges diffuse. Therefore, a smooth Gaussian transition has been implemented. with an approximate range of 4 micro to 5 micrometer has been implemented on the surface of each region. The error will be below a 2 % in this case. Another reason to avoid $f_s(r)$ is the computing resources that are spent to solve exponential equations. Solving sigmoid functions increases the simulation time, and there will no need to obtain more accurate results if the simulation brings conclusive results.

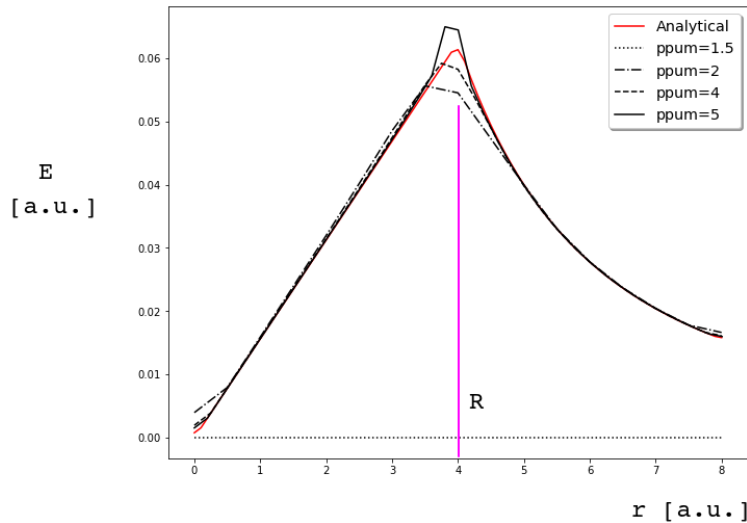


Figure 3.1: Discretization study. An homogeneous spherical distribution was simulated under different $ppum$ (see in the text). The method was used to compute the potential and then perform the gradient of field. We can identify three different regions where the artifacts are present: before, after and near the interface surface. The convergence in the other regions is acceptable, being the maximum discrepancy of 8 % in the region 2.

3.2. Simulation methodology

All the calculations and simulations have been made using an original code¹ written in python and using standard scientific libraries like Numpy [25] or Scipy [26].

The computing strategies were adapted to the different methods to calculate the fields. In the case of the electric field's calculus, it was based simply on brute force. It is the natural way to solve it because we need to add the individual influence of each charge in the discretization of a given volume. With a low $ppum=1$ pts/ μm and the potential calculus instead of the direct field calculus (see eq. 3.4 and eq. 3.5) it is not needed to include the $f(r)_s$ as a sigmoid function. Instead we only add the rule to the program that $V(p, r = 0) = 0$, avoiding infinite terms. As $f(r)_s$ expression is complex (exponential

¹The project simulation software can be found at <https://bitbucket.org/cqs00/electric-potential-3d-sensors>. Currently the software access is private, but you are always welcome to send me an email if you want access.

calculations are needed) avoiding it reduces the computing time. Note that having $r = 0$ means that the charge distribution and the simulated volume overlap, fact that implies that the discretization must be the same for both.

The case of the weighting potential is different. The iterative process has to search for the maximum residual in each iteration. If the total number of points is elevated it will cause an increment of the search time when we sample all the volume. Therefore, it requires an algorithm for a faster search. Our search algorithm is based in the way the iteration and new potential assignments work. As the residuals changing between iterations are only those near the new potential points, it is only needed an initial residual calculation for the full volume. Then, for each iteration we update the residual that have changed. As the volume is defined by a parallelepiped mesh grid, during the first search we store the maximum values of the elements in one dimension and its index. This gives us as result two matrices with the maximums and indexes, upon which we do the same trick. We got two vectors (values and indexes) ending with the total maximum and the index in the vector. Every time we change a value, we must recalculate the residual of its first neighbours and actualize the algorithm values if the new residuals are higher. For example, if we simulate a cube of 100x100x100 points in our first step we have to search among all the 10^6 points. In the second iteration we need to search once in the vector, once in a row of the matrix and once in the column of the distribution which leads a search in only 3x100 elements. Search that is reduced if the distribution has some type of symmetry. The time we spent actualizing the algorithm elements is several orders of magnitude lower than a full search. It is translated into about $1.4 \cdot 10^4$ iterations per second in a standard PC (without symmetry). As mentioned in the previous section the weighting potential calculation has to stop at some point. In this simulation the tolerance was not chosen at the beginning, it as been decided that the simulation had to stop when the behaviour of the weighting field lines follow a patter similar to other simulations in 2D distributions [27], and has not artifacts. At this point calculating the fields is trivial if we go though their gradient.

The next step would be the generation of the transient currents (signals). To solve all the cinematic equations of a charged particle generated inside a pixel, three parameters are required: the charge of the particle q , the initial position p_0 and the particle's mobility inside silicon μ . This simulation does not intend to reproduce the interaction of an interacting particle with matter, therefore they are created at a given point p_0 . With the equations, it is easy to compute $p(p_0, E)$ ad $t(p)$ that will be needed later to calculate the transient current in the electrode $I(t)$, using RST, generated by the charge carriers while drifting inside the bulk. The charge carriers movements, p , are evaluated at small steps (n) of longitude l in the direction defined by E .

$$p_n \simeq p_{n-1} + l \frac{\vec{E}_{n-1}}{|E_{n-1}|} \quad (3.6)$$

The time spent is proportional to the velocity v that can also be expressed as function of E .

$$t_n \simeq t_{n-1} + \frac{l}{\mu|E_{n-1}|}, \quad t_0 = 0 \quad (3.7)$$

By modifying RST to include the effect of magnetic fields we will be able to study its influence in the sensor response, in particular charge sharing. Charge sharing, as its name indicates, is a process where one pixel recollects charge generated in another pixel.

Under normal conditions the electric field lines are enclosed within the pixel cell due to the architecture of the 3D pixel. If a charge generated inside a pixel has not external influences it will be collected by one of the electrodes of the same pixel. There is still ways to produce charge sharing. For example, there is a type sharing mediated by diffusion. If several charges are generated very close to the limits of a cell, the interaction between them (Coulomb repulsion) could push some of them to the adjacent pixel [28]. Another example will be the presence of a magnetic field. The force of Lorentz can modify the force field depending on the magnitude of the field itself and the behaviour of the \vec{E} lines. That is precisely one quantity which our project aims to quantify: the charge sharing magnetically mediated. To do this, a first method is to measure the volume of the pixel where any charge that could be placed will be collected by another cell. This sharing volume is normalized with the total volume of the pixel. Sometimes, we will not refer to it in percentage terms, but in terms of *deepness* instead. Deepness is defined as the distance between a pixel edge and the considered point of the neighbour pixel. As the charges have to cross one of the surfaces that limits the pixels, we can elaborate maps according how deep a charge is migrated.

Depletion voltage is also another parameter to characterize the semiconductor and evaluate the validity of the simulation. As our method of electric field generation assumes that all the ionized charges are sources of the electric field, this situation implies that all the volume is exactly fully depleted. The obtained potential is equal to the potential we would obtain if a bias voltage were applied just enough to remove the charge carriers from the semiconductor. This is a condition derived from the method. We can not control V_{bias} as a b.c. to solve the problem, but it can be introduced by other methods. However, this state in which the system finds itself offers an opportunity to study sensor depletion process. Depletion voltage can not be identified as the maximum difference in potential inside the detector. But once we obtain the field distribution we can compute all possible paths a drifting particle. The difference of potential can be calculated from the electric field lines a particle will follow:

$$V_A - V_B = - \int_A^B \vec{E} \cdot d\vec{\ell} \quad (3.8)$$

The maximum difference of all possible paths is will be the depletion voltage. We choose the starting points that define any type of line as a whole. Any other line that can be chosen will have intermediate properties. This implies that the line containing the last point to be emptied (which will define V_{dep}) will be contained in our selection. The other approach requires more computation time but will describe the depletion process as function of the bias voltage. In our case, we considered that 1D profiles of the depletion will be enough to characterize the process.

Chapter 4

Analysis and Results

The analysis and results obtained in this project are discussed in this chapter. We will show the charge profiles used as input of the simulation, the obtained maps for the electric field inside the pixels and the weighting potentials and fields. Those ingredients allow us to simulate the induced transient signals when an ionizing particle impinges a 3D silicon sensor. A discussion and study of those signals is presented, and compared when the pixels are under a magnetic field influence, quantifying its charge sharing.

4.1. Doping profiles

The electric field inside the sensor's bulk (created by the fixed impurities of the doped silicon) is evaluated by solving Poisson's equation using the equivalent charge distribution method described at Section 3.1.2. Therefore, the doping profile of the different elements of the pixel cells are crucial to obtain a realistic simulation of the electric field. The input doping profiles have been obtained from the real profiles used in the last fabrication campaign of 3D pixels at the IMB-CNM foundry¹, and are shown in table 4.1 and in figure 4.1.

Cell region	Impurity type	Impurities density [cm ⁻³]
N-column	n ⁺⁺	1 · 10 ²⁰
P-column	p ⁺⁺	1 · 10 ¹⁹
Bulk	p	1 · 10 ¹²
Back-end	p ⁺⁺	1 · 10 ²⁰
P-stop	p ⁺	5 · 10 ¹⁶

Table 4.1: Input doping profiles used in the simulation of the electric field. The values have been obtained from the last fabrication campaign of 3D sensors at the IMB-CNM facilities. The number of impurities per cm³ are shown for each element of a pixel cell, along with the type of doped impurities. Each region can be clearly identified in figure 4.1, showing the same information but in a graphical representation.

The entire volume of the pixel cell has been generated with a mesh of equally spaced points, where each point is assuming the equivalent charge which corresponds to the den-

¹Internal communication with Dr. Salvador Hidalgo and Dr. Giulio Pellegrini, Institut de Microelectrònica de Barcelona-Centre Nacional de Microelectrònica

electric field should be compensated. There are other regions in the opposite situation. Looking at the doping profiles (fig. 4.1), it can be observed points with strong charge transitions, therefore rising the electric field. In fact, the field ranges from 420 V/cm to 1 V/cm, with large variation regions.

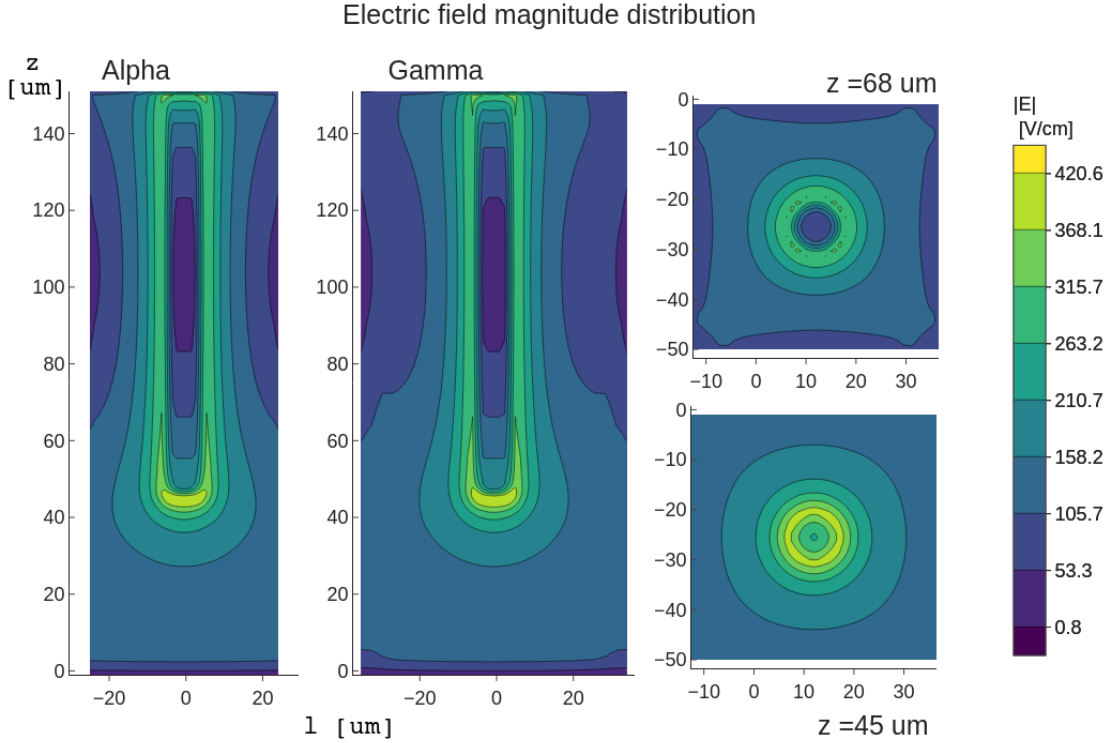


Figure 4.2: Electric field absolute magnitude for 4 different sections of a 3D $50 \times 50 \times 150 \mu\text{m}^3$ pixel cell geometry. The figures shows the most representative vertical planes of the detector (alpha and gamma) and two examples of the field at two $z = 45 \mu\text{m}$ and $z = 68 \mu\text{m}$ values. The columns occupy a volume in the center. The two z cuts shows two sections of interest that where selected according alpha and gamma profiles. The two regions of interest are the transition where the n-column ends and the stable region at half of the same column. The electric field obtained varies from 420 V/cm to 1 V/cm.

This fact is also well defined at figure 4.2, where the colour of the path-lines indicates that the maximum values of the electric field are near the columns, being the Gaussian-like charge diffusion its causal factor.

The region below the end of the n columns is also a region of interest. The electric field magnitude in there trends to be larger there than in upper z cross-sections. This under-column section has in average the same distance to the p columns, but it is closer to the back-plane than to the n-column, therefore the E values in there are strengthened.

Still in this low z -regions, the strong doping of the back-plane hides partially the effects of the continuity leak in the sensors, in the transition between the air and silicon (top and bottom). Even so, in the regions of the bulk near the top we can see a trend change of the field to go slightly up. The discontinuity behaves like if in the bulks limit would be a positive charge distribution, deflecting the field lines. In this region we could see charge losses.

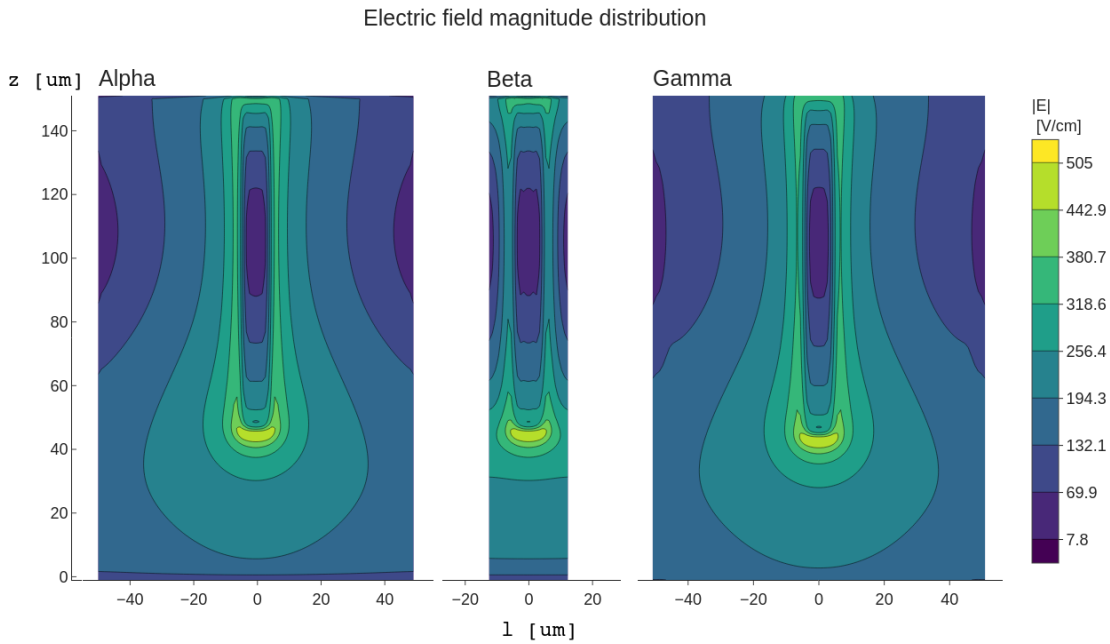


Figure 4.3: Electric field absolute magnitude for a $(25 \times 100 \times 150 \mu\text{m}^3)$ detector). This geometry offers an additional plane for study compared with the previous detector. A strong change in the behavior of the electric field in the beta direction can be observed. The z sections are presented in figure 4.4. The electric field obtained varies from 505 V/cm to 8 V/cm, being a little higher than the values of the other pixel.

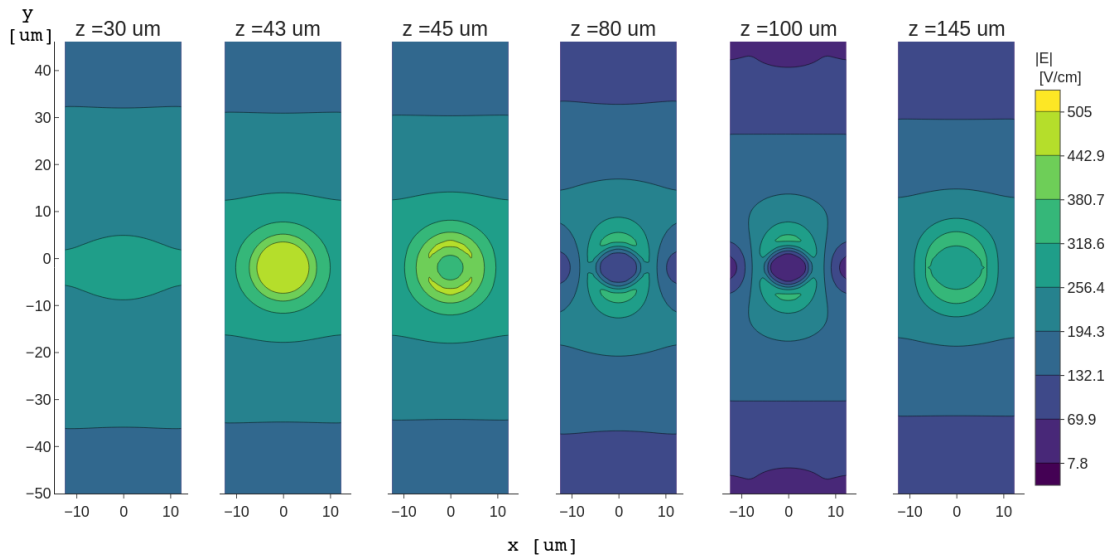


Figure 4.4: E field magnitude at different values of z ($25 \times 100 \times 150 \mu\text{m}^3$ detector). This row of sections compared with those presented in figure 4.3 gives a 3D understanding of the electric field behaviour. From down to up the field iso-lines gradually appear until the maximum values is reached at $z \simeq$. Going up, that values will not be reached again.

The case of the of the $25 \times 100 \times 150 \mu\text{m}^3$ configuration presents some particularities due to its rectangular, then not fully symmetric, shape. We can introduce another cut of interest (see β at fig. 4.3). Whereas the electric field in α and γ sections behaves like in the other configuration, the β shows different patterns. The short distance between the neighbour n-columns modifies the field lines at low z . Instead of having a *bulb*-like shape present in the other directions, the field is flattened. The field in there resembles what is produced by a charge wall. The slice selection performed at different z values also shows the influence of those short distances between the n-column of the adjacent neighbour.

Charge carrier's drift calculation becomes straightforward at this point. Figure 4.5 shows the field lines, and therefore, the particle paths that electrons and holes follow after their generation. With no magnetic field electrons and holes follow the same paths but in opposite directions. Electrons are collected in the central columns, but holes can be collected at the p-columns or at the back-end, depending their point of creation. Note that figure 4.5 is showing just the case of being collected at the p-columns.

The p-stop ring has not a significant effect in the charge carrier drifting. The doping value is not enough to counteract the strong attraction of the columns. Its influence is so small that it is not distinguish from the case when the p-stop is not included in the simulation.

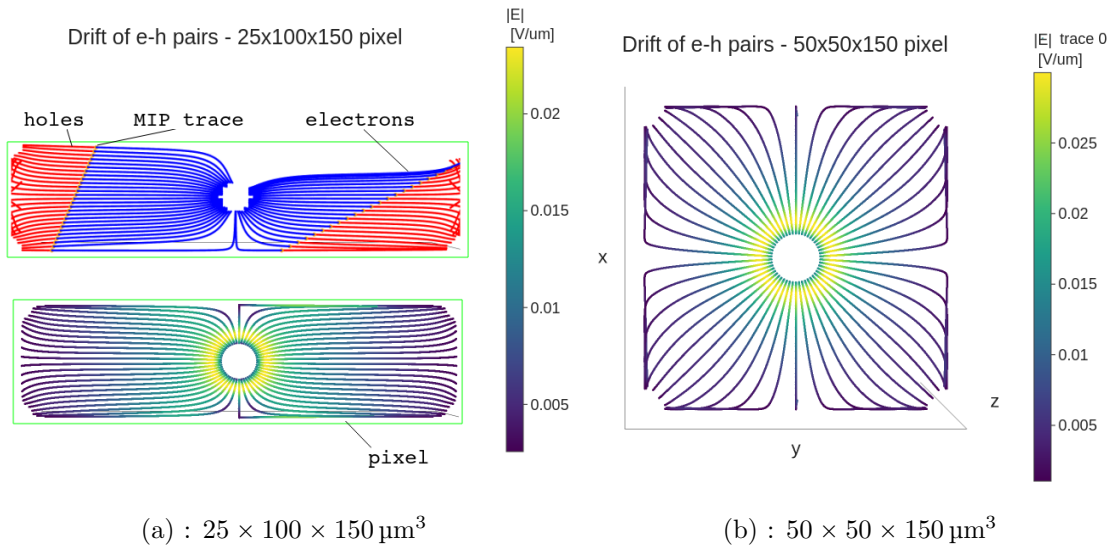


Figure 4.5: Electric field lines for the two pixel studied configurations. Figure (a) represents a full set of the field lines associated with their field magnitude. It also has included an interaction of two MIPs with the sensor. The interaction is represented as orange dots, where the electron and hole pair are generated. The red (holes) and blue (electrons) lines shows the drift movement until they are collected by their respective electrodes, electrons drift to the n columns whereas holes are collected at the p columns. Figure (b) represents the electric field lines for the other cell configuration.

The electric field profiles are compared with the few available literature [10] and with private results from 3D foundries² and they agree with the TCADs models used in there. The charge distribution approximation method is indeed a powerful, yet enough accurate

²Internal communication with Oscar Ferrer, IMB-CNM.

simplification allowing to largely reduce computation times.

4.2.1. Depletion voltage

Another parameter that defines our simulated detectors and we can estimate, is the depletion voltage V_{dep} . As it was already explained, the analytical resolution of this value is not possible with the used method, but can be easily estimated by evaluation of the path integral of the charge carrier from two extreme points (eq. 3.8) as discussed in section 3.2. The maximum difference will be identified as the V_{dep} . Due the geometry of the sensor, we have opted for following the paths starting away from the n-column electrodes, simplifying the study of the depleted volume.

Figures 4.6 shows the potential difference between the two ends of the electric field lines for the square pixel configuration. In that figures, the paths of charge carriers created near the p-column or the back-plane, and following different electric field lines will allow us to evaluate the depletion voltage. The voltage difference has a minimum value of 0.38 V at $z \simeq 100 \mu\text{m}$. For larger z , the influence of the detector's interfaces increases this value, whereas in the opposite direction the discontinuities of the back-plane and the n-column's edge has a similar effect. There is a sharp transition in the behaviour of the field lines that end in the central column, so being this z-section the region which needs larger energy in order to be depleted. In the figure, two different types of field lines are represented. Those starting from the p-columns and those starting from the back-plane. The latter show larger depletion voltages in part because in its way to the n-column, they travel along different z-values, so larger distances than its counterparts at $z \neq 0$. The maximum value obtained is $V_{dep} = 0.91 \text{ V}$, which is compatible with measured values [8].

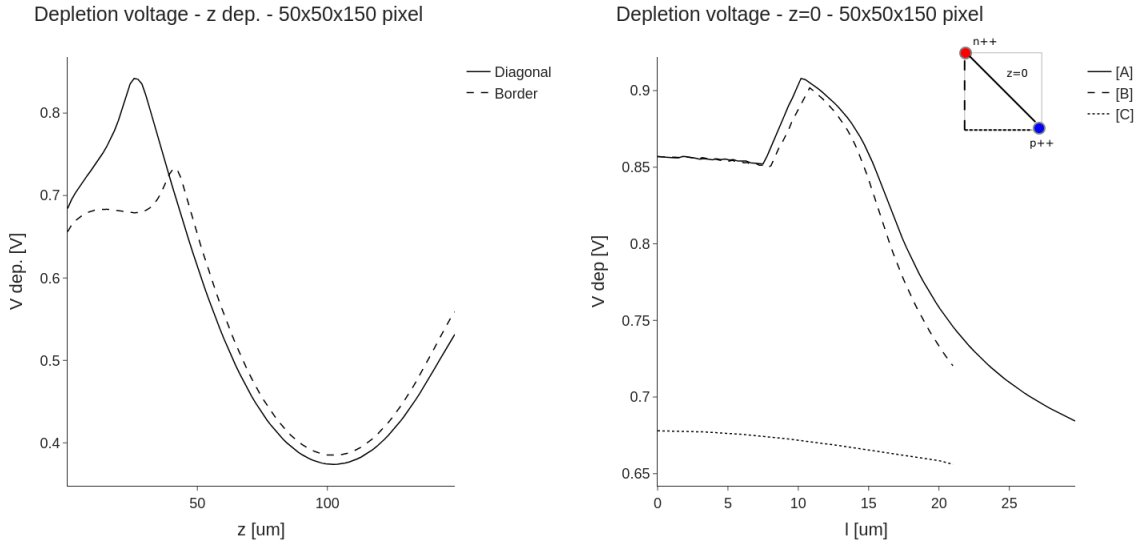


Figure 4.6: Potential energy voltage calculated at different electric field lines, used to calculate the depletion voltage. Probe charges are placed on the p-column at different z (left plot), or near the p-column at different distances to the back-plane (right plot), and travel following a path near the border of the pixel, or the diagonal. Study performed with $50 \times 50 \times 150 \mu\text{m}^3$ configuration. The maximum voltage obtained is 0.91 V.

The same study can be applied to the $25 \times 100 \times 150 \mu\text{m}^3$ pixel configuration. How-

ever, the rectangular shape introduces a more complicate behavior than the parabolic-like dependence shown in the pixel square configuration, as it can be observed in figure 4.7, with a richer structure. The field lines starting at a p-columns are a two-factor larger than in the rectangular case, and therefore, the potential should be larger as well. The extremely different charge densities between the short distance of the rectangle, creates large potential differences, and therefore, modifies the behaviour of the V_{dep} with respect the square case. We can observe when studying the p-columns starting lines, that depending the region the depletion voltage has very different z-dependence between them. The asymmetric geometry could explain those differences, although we did not further proceed with a deeper study. It is planned to explore and deeply understand these dependencies in future studies. The depletion value obtained agree in magnitude with measured detectors [8], $V_{dep} = 1.32$ V.

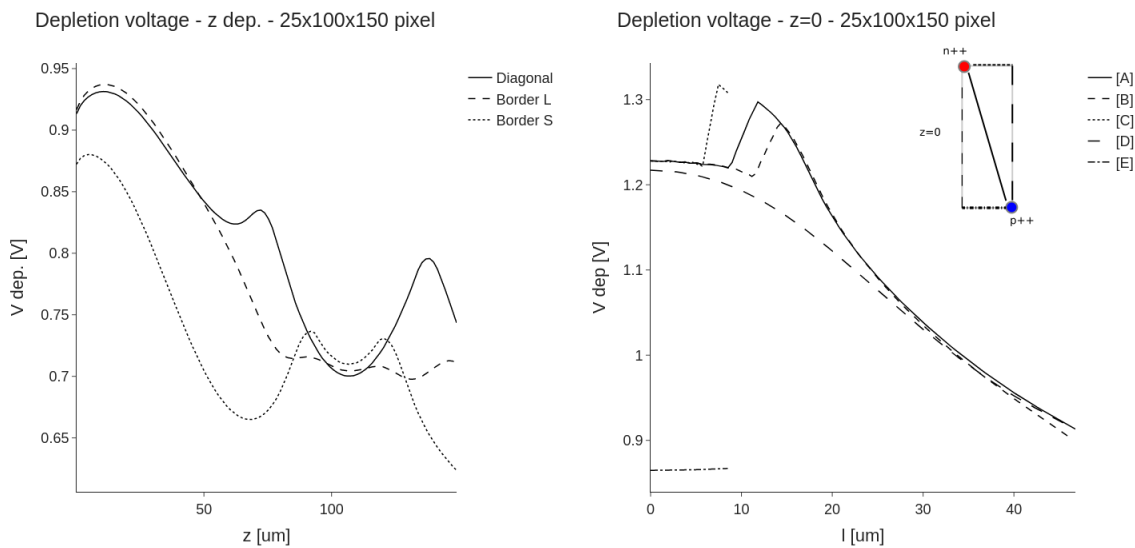


Figure 4.7: Potential energy voltage calculated at different electric field lines, used to calculate the depletion voltage. Probe charges are placed on the p-column at different z (left plot), or near the p-column at different distances to the back-plane (right plot), and travel following a path near the short, the long borders of the pixel, and the diagonal. Study performed with $25 \times 100 \times 150 \mu\text{m}^3$ configuration. The maximum voltage obtained is 1.32 V.

4.2.2. Weighting field.

The last element to calculate allowing the transient current simulation is the weighting potential, the mathematical figure which encapsulates the geometry description of the induced current problem. Figures 4.8 and 4.9 show the weighing field for the two considered pixel layouts.

The potential falls in an exponential-like trend from the central electrode to the other, establishing that electrons are the relevant charge carriers in this system (p-doped bulk, n-columns collecting electrodes). The closest the charge carrier is from the n-column, the more contribution has in the induced charge. An aligned observation: the low z-value region, where the n-column is not present, is also a negligible region to contribute into the

signal.

The three-dimensional nature of the problem makes difficult to visualize weighting potential dependence with the position of the created charge carrier. Figures 4.10 helps in analysis by showing the weighting potential values with respect the position of the charge carrier, where it is emphasized the larger contribution to the signal of those carriers near the n-column with respect farther regions, and in particular z-low regions.

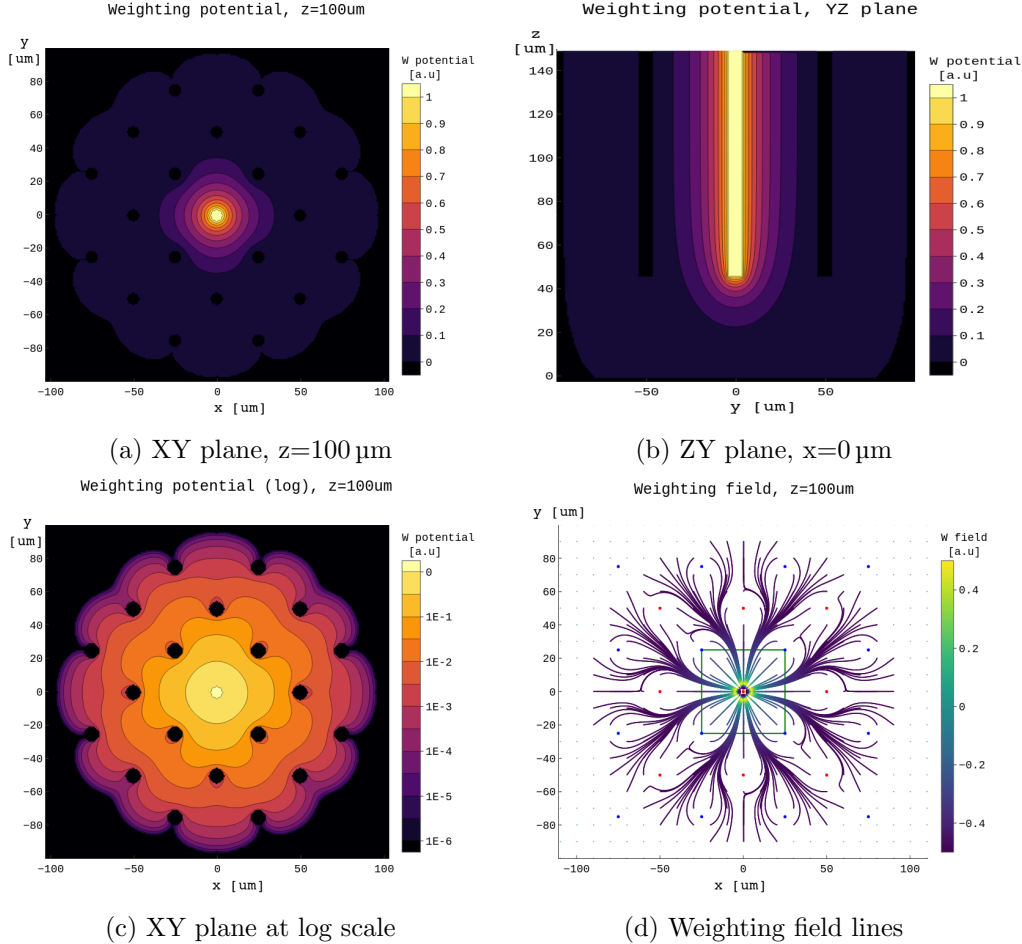


Figure 4.8: Weighting potential and field comparison. Figures (a), (b) shows two isolines maps of the weighting potential ($25 \times 100 \times 150 \mu\text{m}^3$ detector). For a better understanding, the isopotential distribution has been represented also in log scale at figure (c). The field (d), in contrast, remains in linear scale showing clearly the large drop in potential. Columns location are marked as red (n-columns) and blue dots (p-columns), and the central pixel cell limit is represented by a green line. The relation of figures (c) and (d) becomes clear if we note that the field lines are perpendicular to the potential isolines. The field lines are collected by the central electrode (set to 1 V) and originated in the others (set to 0 V).

4.3. Transient signals.

The induced signal due to the drifting of charge carriers will contain the information of the pixel itself and also of the ionizing particle, more specifically the path than the ionizing

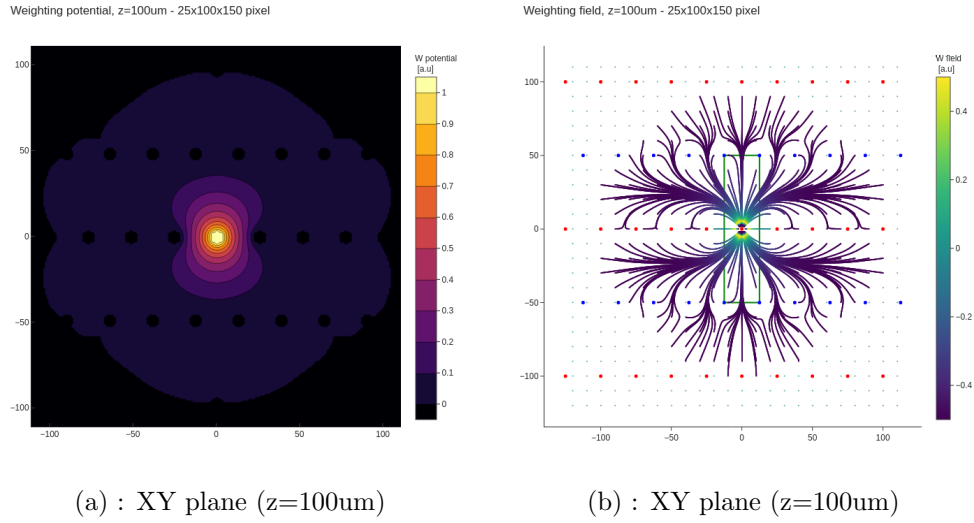


Figure 4.9: : Weighting potential (a) and field (b) for $25 \times 100 \times 150 \mu\text{m}^3$ architecture. Red dots represent the p-columns and blue dots, the central n-column. A pixel cell is delimited with a green line.

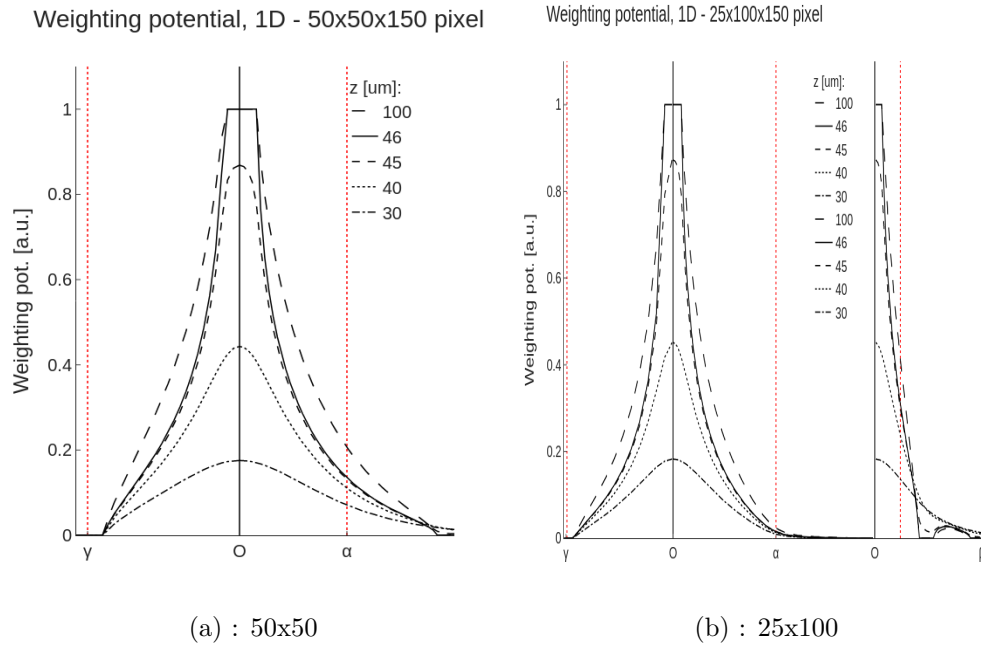


Figure 4.10: : Weighting potential's one-dimensional profiles of the two detectors in the main directions. A set of different layers (z dependence) is represented. Pixel limits are marked like red lines to show where the field extends significantly to the adjacent pixels. This profiles do not correspond to field profiles, which exponential-like behaviour determines in addition to the electric field the signal profiles.

particle follow. However, as the particle-matter interaction is not simulated in this work, we are focusing on the study of the induced transient signal with respect to a creation point. In such a way, we present a brief study of some of the most significant cases. This allows us to identify the most important aspects in signal generation through the drift of the charges generated during the interaction with one or several MIPs. The analysis will be extended to consider the effect of magnetic fields on charge migration.

Once the electric field, which determines the velocity and paths of the charge carriers, and the weighting field, which weights the induced signal, it is possible to simulate the response of the pixels. Talking about response is the same as saying signal induction (I), as RST proved. Figure 4.11 compares these two fields with the response of the detector. The response is scalar product of the two fields. As we anticipated during the study of the fields, the place where the most signal is generated is near the n-column. Three effects contribute to this fact: the high value of the electric field, the high value of the weighting field, and the relative orientation of the field lines. The comparison of this figure was performed in the $25 \times 100 \times 150 \mu\text{m}^3$ configuration because this last point is more evident, however this is valid also for the square layout. The field lines have a similar orientation except in the β direction, where the presence of the next columns have the opposite influence. In this orientation the charge induction is weaker than in α . The weighting field also has a great influence at large distances far from the central column.

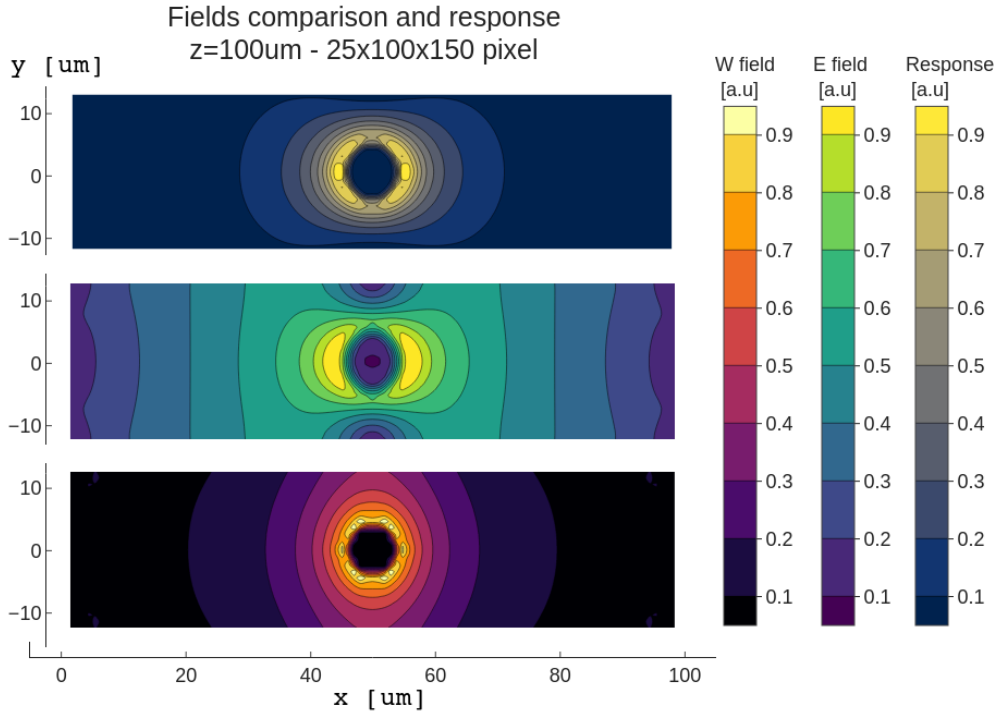


Figure 4.11: Fields comparison and relative response (induced charge) ($25 \times 100 \times 150 \mu\text{m}^3$ pixel). The figure shows three sections of the pixel in the xy plane ($z = 100 \mu\text{m}$), representing the weighting field absolute magnitude, electric field magnitude and the response in arbitrary units. The response is shown to be determined (RST) by the behaviour of both fields.

The large casuistic available to study the transient signals, force us to choose several paradigmatic cases. As starting point, we simulate a single electron-hole pair production at an arbitrary point to cross-check the simulation framework: the total induced charge must be recovered from the induced transient current to be the initial created charge. This is shown in figure 4.12, where we integrate the transient signals and recover more than the 99.5% of the created charge, which is within the errors and tolerance, validating our procedure.

The holes' drift is slower than the the electron's drift due the difference in their mobility which results in two assessment: the contribution of the holes to the signal is longer in time (at equal path distance) and the intensity is lower in the same proportion due to RST. When the electron and the hole are close (at the beginning of the signal) they feel approximately the same field, so the ratio between their contributions is exactly the ratio between their mobilities. The hole is always moving towards low field (electrostatic and weighting) regions, thus its induced signal is weaker, and slower.

We can see that electron and hole contribute positively in the generation of the signal because the sign of their charge is compensated with the sign of their paths direction (RMS - scalar product). In this case, the path of the electron through the field line is very similar to the direction of the weighting field in each point.

Comparing figures 4.8 and 4.5 we can note there are paths that follow trajectories that are almost perpendicular to the weighting field. In this situation, independently of the fields' magnitude, the obtained signal will be minimal.

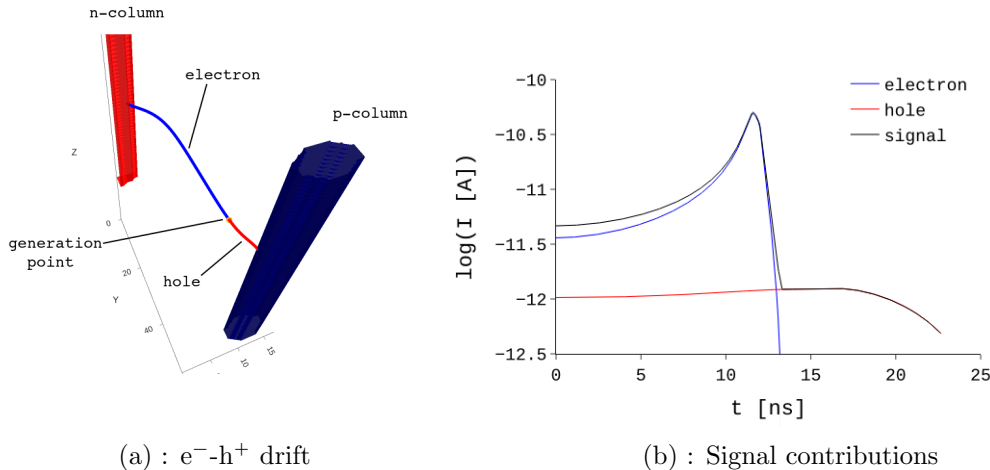


Figure 4.12: Example of transient currents. A single e-h pair generation has been evaluated. Figure (a) shown the generation and drift of the electron (blue) and the hole (red), and its generated transient signal at (B).

If a MIP is simulated to cross the detector, just by creating every micron some e-h, the charge carriers will create mixed contribution on the induced signal. For example, in figure 4.13 have the signal produced by a MIP registered in two pixels, the central one and one of its neighbours. The circumstances are similar to the last case, where the MIP pass closer the p column. The resulting figure (a) looks similar to the single e-h transitory pixel but the figure (b) does not, where it is showing the transient signal in the neighbour pixel where the charge carrier was created. This is a bipolar signal, as the charge is not going to be collected in the electrode and therefore the integral of the transient signal should be

zero. In other words, we can only expect transitory signals with polarity inversion if some of the charge is not collected by the reference electrode.

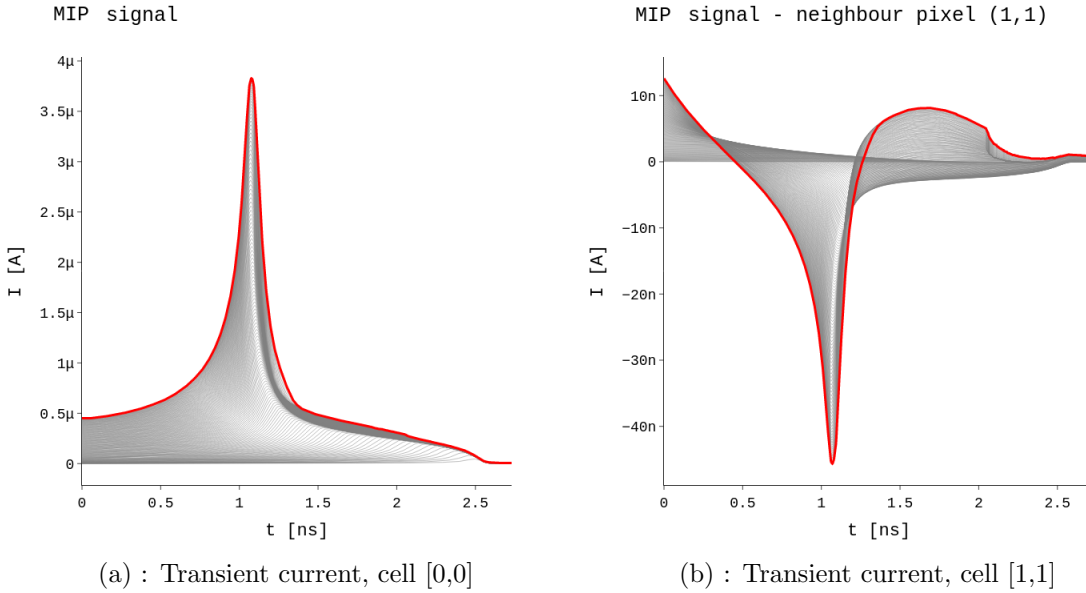


Figure 4.13: Example of transient currents for the square pixel geometry. A travelling MIP has been simulated, crossing the detector vertically ($x=y=18\ \mu\text{m}$ from the center). Figure a contains the induced signal in the central cell ([0,0]) whereas b shows the same for the signal induced at the first pixel diagonally located ([1,1]). The red line defines the overall signal whereas the gray lines shows the individual contribution of the charge packets that the MIP generates.

The study of the full transient signal of the created e-h along a path of a MIP resembles the one of an unique e-h pair. A deeper look, see figure 4.14, illustrates the low contribution of holes to the signal. Actually, this tail is caused by electrons that move at low z , where there is not n column and the electric field is weaker. This "lazy" electrons move slower than those generated in higher layers, retaining the shape but weaker and shifted. This is represented by the coloured areas in the left figure 4.14, where blue is the signal induced by e-h created at z above the end of the n column, and yellow for those beneath the column. Clearly the signal intensity is dominated by the fast electrons at first, situation that inverses at the end. This pure simulated signal could be passed through a frequency filter to simulate the limitations of a real setup, like figure 4.15 shows.

In the case of the $25 \times 100 \times 150\ \mu\text{m}^3$ pixel, the transient currents have similar profiles and also polarity inversion. However, the ratio between the absolute maximum of the two signals largely differs from the previous case. The ratio is approximately 0.01 (45:4000) if we look the $50 \times 50 \times 150\ \mu\text{m}^3$ signals and 0.10 (250:2500) in the $50 \times 50 \times 150\ \mu\text{m}^3$ signals. This result was also expected. Next pixels located along β direction will register a transient signal greater in that configuration because the weighting field lines predict it. To complete the signal study we have simulated and compared several transient currents generated by MIPs passing at different points of the cell, always parallel to z , as they can be seen on figure 4.17.

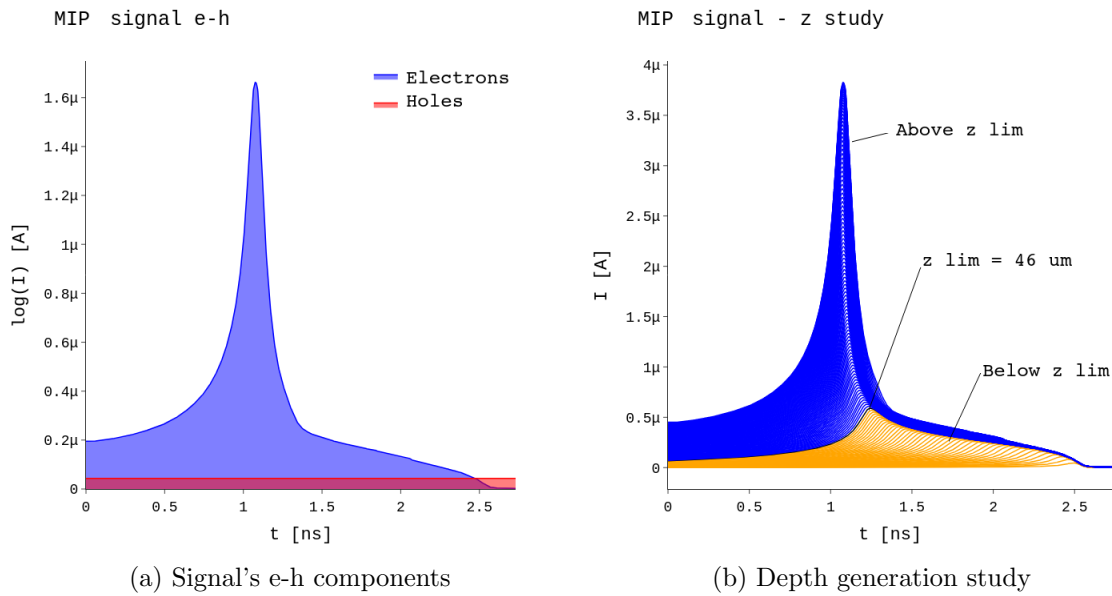


Figure 4.14: Study of a transient signal. Both subfigures were simulated under the same parameters than fig. 4.13(a). The figure shows the electron-hole current contribution and the dependence with the depth (z). Figure (a) shows that the main contribution to the final signal in terms of charge carriers are electrons. Figure (b) shows, as the MIP crosses in the z direction the detector, the contribution of the charges generated above and under (blue and yellow respectively) the layer where the n column ends.

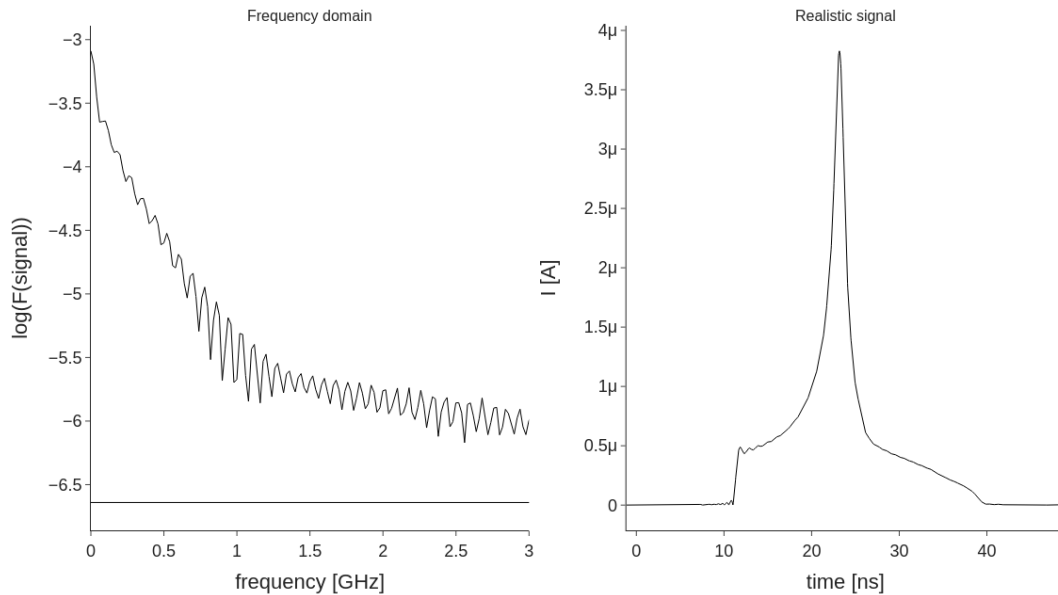


Figure 4.15: Realistic transitory signal. Under real working conditions the transient signals differ from the simulated ones. This occurs because there is a cut in frequencies when the signal passes through the different electronic devices in charge of collecting it.

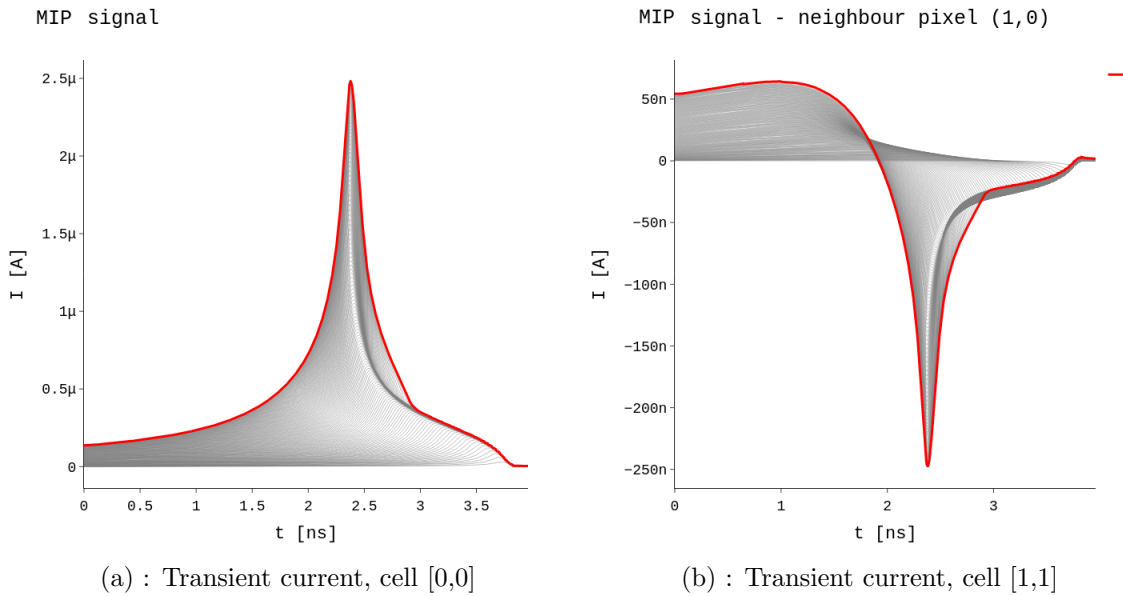


Figure 4.16: MIP transient signals on a $25 \times 100 \times 150 \mu\text{m}^3$ pixel. The time and profiles change from the squate configuration due to the strong dependence with the creation point and the geometry of the pixel.

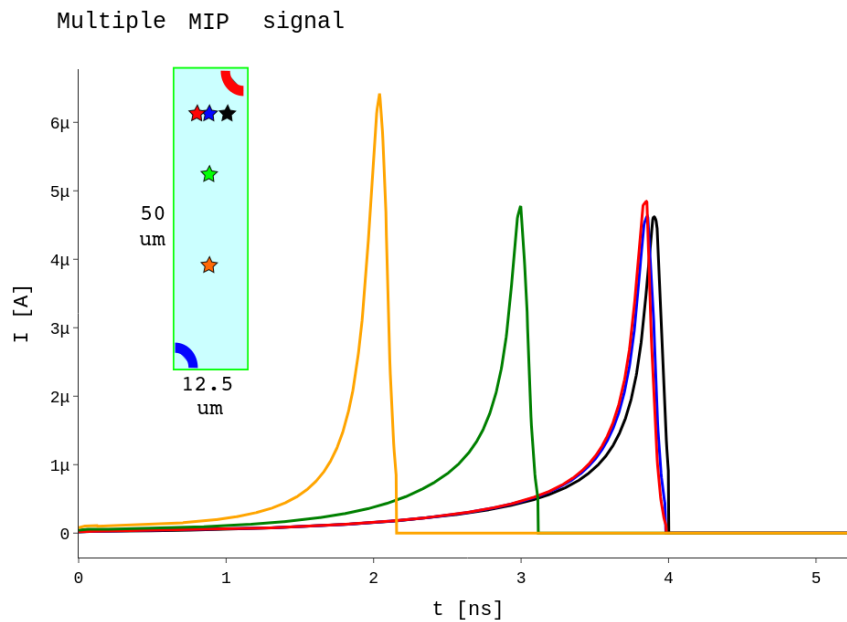


Figure 4.17: Multiple transient profiles. Simulation of five transient signals generated by MIPs with different trajectories (always parallel to z).

4.3.1. Under magnetic fields.

As it was said, the CMS sensors work under high magnetic fields. This field can reach up to 3.8 T under normal operation, value that has been chosen to assess the migration of charges. As we saw fig. 4.5, the electric field lines are enclosed in the pixels' limits but flow parallel and near to them in certain locations. This means that a magnetic field, no matter the intensity, will cause charge sharing in a given amount. The value of 3.8 T is not enough to produce a significant effects on the path of the electrons and holes so it is necessary to map the volume with a precision that would require too many resources in terms of time, without giving any new information (see figure 4.22). Instead, a maximum limit of charge migration has been establish. The surface that determines the border of each pixel is different for each pixel configuration (3.75 vs 3.0 μm^2). Near it, exists and effective volume where the charges generated can escape under a 3.8 T field. This process takes place when this charges are produces less than one nanometer close to the limit. This means that the total amount of charge sharing is below the 0.001% when the B is applied in the "barrel" configuration ($B = B_z$), and even lower (about one order of magnitude) for the "end-cap" configuration. To observe this effects in more detail it is indispensable to simulate higher values of the magnetic field.

The data obtained by several authors in real experiments using 3D sensors shows exactly the same results we have obtained [29]. Charge sharing by diffusion is a well known process [28], where the electrostatic repulsion between charge carriers allows the migration to other pixels. This charge sharing will not be increased substantially by magnetic effects. It is not expected that the tracking procedures will change only to take into account magnetic effects.

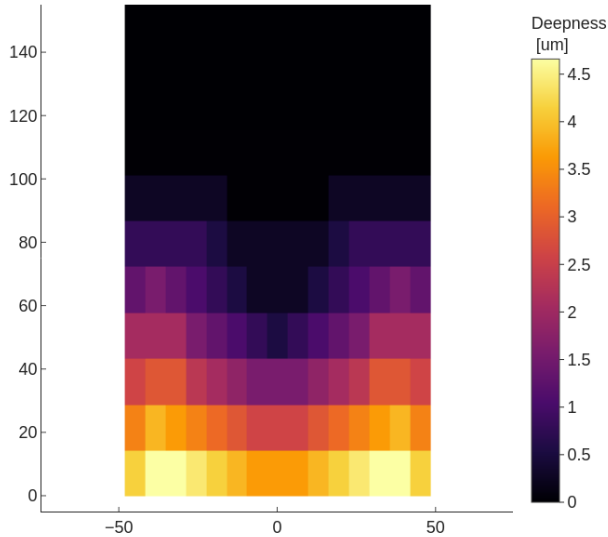
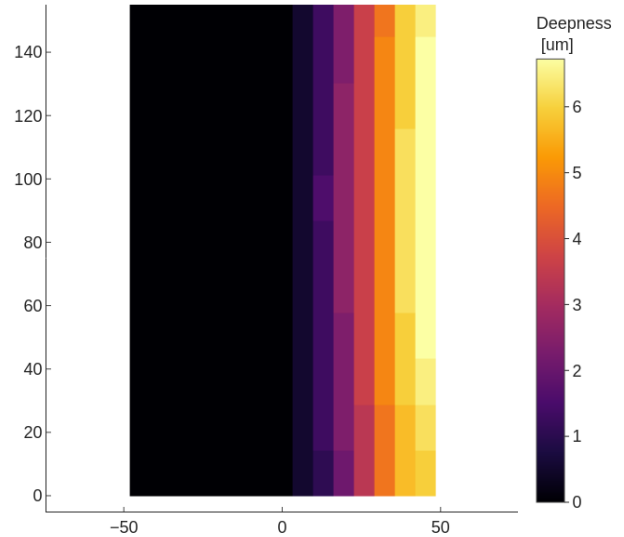
Sharing deepness - $B = B_x$ (a) : $B = B_x$ Sharing deepness - $B = B_z$ (b) : $B = B_z$

Figure 4.18: : Sharing deepness. This 2D map represents the limit in deepness that an electron is stolen from the pixel where it was created when a strong magnetic field ($B = B_x$, $B = B_z$) is present.

Both types of detector have been studied under the influence of B , but is the 25×100 detector the one which brings the most interesting results in a qualitative way. The lower grade of symmetry that it has makes it possible to explore the influence of these fields in more significant directions. For example, in figure 4.20 it can be seen the paths that will follow a hypothetical charge under the influence of different magnetic fields always parallel to a axis. The paths are computed from the p columns' proximity and from the limit between pixels (shorter dimension) at $z = 113 \mu\text{m}$. This has been done in that way because the limitations of showing 3D paths into a plane. As we will discuss later, at z values close to $100 \mu\text{m}$ the detector presents less z -drive and the figures are easier to interpret.

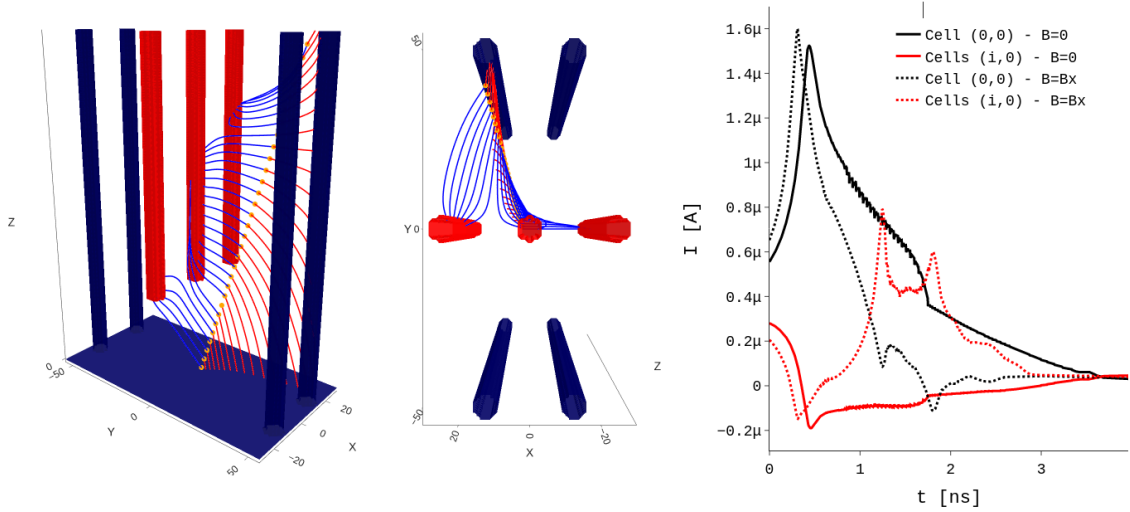


Figure 4.19: Paths of electrons and holes on a $25 \times 100 \times 150 \mu\text{m}^3$ pixel matrix under the influence of a magnetic field $B = B_x = 3 \cdot 10^7 \text{ T}$. The incident MIP only crosses the central pixel. Therefore, the migration of the charges that ends in other electrodes is produced by B . The relative charges recollected to the maximum in both signals are 1 and 0.002 if there is not magnetic contribution in contrast with 0.608 and 0.392 with the already mentioned field.

The magnetic contribution is not a weight factor until the magnetic fields reach approximate values over 10 kT . Even higher fields (of $B = 10 \text{ MT}$ and $B = 30 \text{ MT}$ for the $50 \times 50 \times 150 \mu\text{m}^3$ and $25 \times 100 \times 150 \mu\text{m}^3$ respectively) are needed if a value over 35% of charge sharing want be reached. Thus, obtain similar results on real experiments is out of mind. This means that we should not see magnetic effects on the signal generation, at least none by this mechanism.

Even so, the magnetic effects in charge drift that we can see are interesting in a qualitatively approach. Under a certain level we start to see charge sharing between adjacent cells. This can be done by two ways: study of the charge's drift path under the force field or integrating the total charge recollected by each pixel.

Since the force affects more electrons than holes and the signal intensity is also dominated by the electron induction, we thought that in the limit of the magnetic effects only electrons will contribute significantly. This is not fully true because as it can be seen in figure 4.19 there is also an important hole contribution due the direction of the trace. Attending to the paths it is clear the existence of charge migration between cells. Part

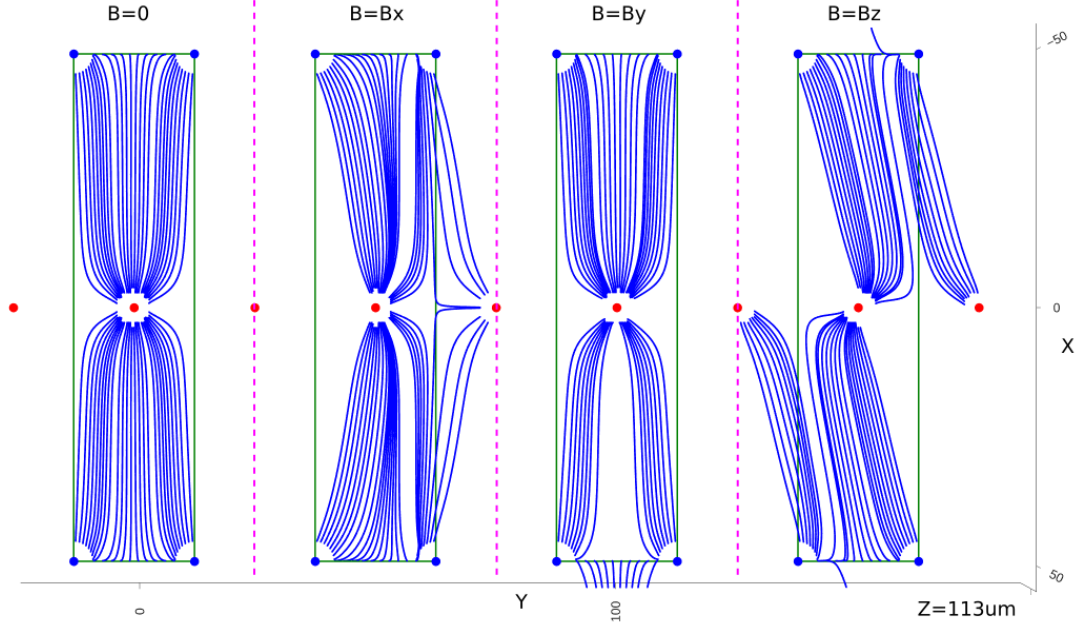


Figure 4.20: Magnetic effects on the $25 \times 100 \times 150 \mu\text{m}^3$ pixel detector. This figure shows the charge sharing between adjacent pixels when the magnetic fields reach a certain level. An specific layer has been chosen to avoid as much as it was possible the Lorentz drift in z . This decision was taken only to simplify the interpretation of the results.

of the electrons are not being recollected by the central column but for the others. The holes, because of their mobility, are not affected in the same way by the magnetic field, not being able to pass to the next pixels. The different behaviour of both charges can also be seen in the points where the e-h pair are generated. Instead the continuous path that we were used to find, now we have a vertex because the rotational component of the Lorentz's force. This abrupt change means that the initial direction of a pair of charges is not the opposite, and the already mentioned ratio between the two current contribution is lost. In the same figure it is also represented the transient currents in the central pixel and in the next ones in the situations were there is and there is not magnetic field. With no B the transient currents have the profile that we expected, similar to the previous ones. In this case the force lines are contained in each pixel and go relatively straight to the electrodes, making also as we expected impossible to recollect charge in the pixels where there is no e-h pair generation. The recollected charge in the two next pixels is about a 0.2 % smaller than the collected in the central one and is compatible with zero. This is precisely the situation you would expect from a 3d detector. The situation is the opposite when there is a strong magnetic field (in this case of $B = B_x = 30 \text{ MT}$). If we integrate the current of the transient profiles and we compare with the no B case we obtain a recovery of a 60.8 % in the pixel with the trace and a 39.2 % in the others. There is charge sharing and there is not lost charge. Both profiles have now polarity inversion (corroborating again the charge migration) and have a triple peak structure. The first peak is produced by electrons collected at cell(0,0), electrons that follow the minimum distance to any electrode so they are collected earlier. Then, the electrons that have migrated to another cells are collected, producing the next two peaks because they are collected in different electrodes at different

times. This is not the only case that we can find because the bipolar behaviour could be hidden under the collection of other charges, but the integral of the signal is always the recollected charge.

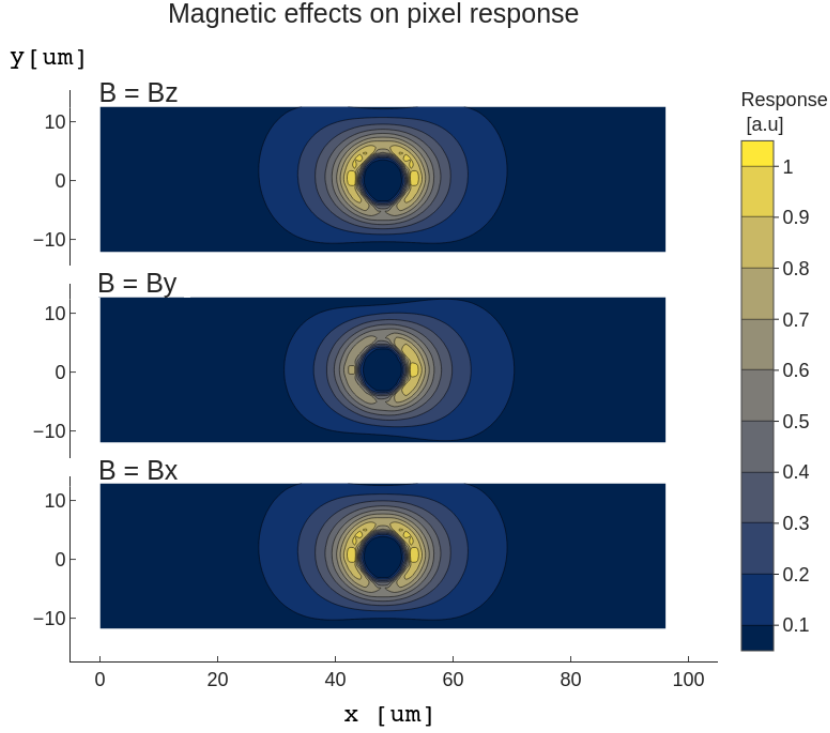


Figure 4.21: Magnetic effects on the response. RST states the relation between induced charge and the velocity of the particle. The magnetic field interacts with the particles changing their drift velocity depending on the orientation of the electric field lines respect to B . This figure shows in a qualitatively way how the response map is affected.

Figure 4.20 gives additional information of the same process. We see that the interacting particle has not been reproduced in a reliable way only to study independently the magnetic effects in different regions. Instead of that, a field representation was considered. The magnetic influence changes according the B direction and magnitude, and how close the charges are generated to the pixel's limit. A good section to evaluate this is a X-Y plane over z equals approximately 110 %. At this value the lower effects of the discontinuities minimizes the z -drift. Magnetic contribution at that level help us to reduce the 3D structure of the field lines and study as the effects were limited to that plane. As it can be seen the symmetries of the field and the pixel are an important factor. When $B = B_z$ the magnetic vector is parallel to the main symmetry axis of the pixel. The charge can escape to the closer pixels. In the $50 \times 50 \times 150 \mu\text{m}^3$ pixel the effect is different from the $25 \times 100 \times 150 \mu\text{m}^3$ pixel as it should be expected. For $B = B_y$ and $B = B_x$ there are still differences between both detectors, but the charge can only be shared with one and only one detector at this level.

If we return to the realistic MIP track we see that this is false. Charge sharing in figure 4.19 shows a z dependence. Internally the changes that this extra force introduces are also relevant, not by the way the charge is collected but the changes on the signal's profile. A magnetic field B_z enough strong can twist the field lines maintaining symmetry, whereas

$B = B_y$ and $B = B_x$ break it.

As we saw for higher fields, there is a strong dependence with the relative orientation between B and the detectors and with the magnitude. Figure 4.20 shows it, because to produce similar charge sharing in x and y orientations it is needed a field approximately four times stronger than the B_z . The qualitative effects are comparable between low and high fields. It is seen that the field lines that star crossing the pixels' borders are not always the same, it depends on the orientation of B too. For example, with $B = B_z$ (at $z \simeq 100$) the charges that are able to escape are those which are generated near the p columns in the limits of the pixel. This is the opposite when $B = B_y$ where the charges that can migrate are located in the middle of the columns. The strong influence that the position of the ohmic columns have in the total electric field is evident.

4.3.2. Experimental limitations

The last point to discuss about is the **limitations** of this project that have a visible impact in the results. Two different types of limitations are present. The first kind are those limitations that lie in the simulation process.

All simulations need a certain amount of time to compute all the instructions that the computers are given. Reducing this time has never been a priority in our work (within the realms of what is reasonable). The total computational time has been long, taking several hours to compute each field. It has a direct impact on the quality of the simulation. Although the code gives the user the option to change the discretization of the detector volume, it will not be wise if the total points are increased further that we have already done. We have been working with a discretization of 1 ppum. This means that the resolution reached is good enough to follow the path of the charge carriers and obtain "clean" profiles, that is to say that no artifacts are generated when the derivatives of the potential were calculated (within an acceptable margin of error). Working under other parameters will be possible in the future because the program is far from be fully optimized. We will adapt this program to decrease the computation times and obtain better results.

Even so, we must put our work in context. Simulations like the ones we are running also require long computational periods, and the programs run on large installations with many CPUs working in unison. If we continue to improve our program and get access to better facilities we will be in a position to beat the times of other simulations.

Now we are limited if we want to search and zoom to obtain more complex information about the transitions between the elements that build the detector. This fact has a relative impact on the establishment of the charge sharing limits because we have concluded a certain amount of charge sharing at 3.8 T, but for that there is a previous process that requires interpolation methods.

The discrimination process of the charges that migrate requires an initial position where the E field is interpolated twice. The first time is performed when the electric field is obtained through the gradient of the electric potential and the second time is performed when the path calculation method is used. The interpolation used has always associated an error that could be consider in the final results.

It was not in our results because the symmetry of the fields in the pixel to pixel transitions. In the case of the electric potential it gives as result an increment of the electric field because the sharp transition but below the discretization it acts as a constant value that changes the way the charges are collected. A similar artifact is generated by the transition between the frontplane and the air. This region could be the worst defined

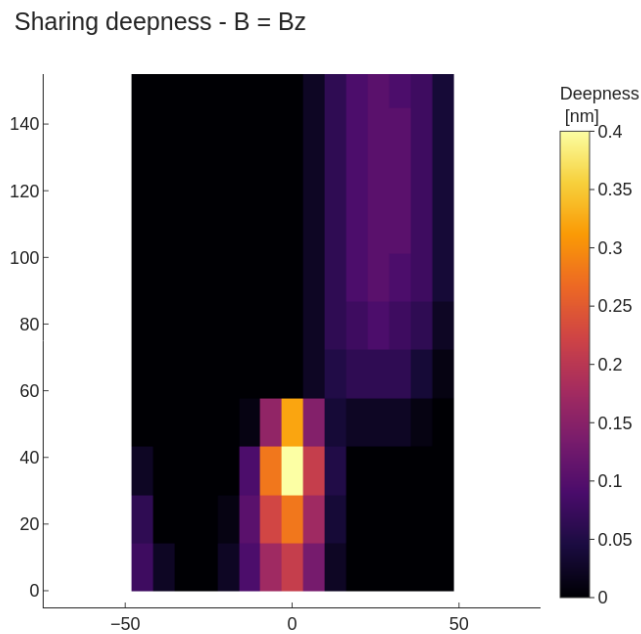


Figure 4.22: Simulation artifact. As figure 4.18 in this figure is represented the deepness at there is still charge sharing. This figure was obtained with a 3.8 T magnetic field. The same pattern was obtained if there was no magnetic field. This artifact is produced by initial asymmetries during the charge assignment according to the dopant levels. The result is that differences are amplified during the simulations, introducing artifacts in the final e field. This produces charge sharing when it was not expected. However, this figure establishes a limit to the sharing process.

because in the top of this artifact we have not included the effects of the elements that are close. Parallelization could be an interesting way to achieve faster and better results, an option that was explored at the beginning of this project, but note that this possibility may not have any effect in terms of time. For example, using this technique to compute the electric field could be a great option due to the independency of the charges at the time to generate the field. In contrast, the relaxational method has to take the data from the previous iteration, and thus, it will be preferable having a single computer with higher computing power.

The other limitations are not related with the resources we could spend. The aim of this work might have been accomplished by many different ways, but the way we chose has its own pros and cons, different than the others. The main restriction is to study the problem as an electrostatic model. It simplifies the equations involved, but we lose all the information of the diffusion and drift of the free carriers during the inverse polarization of the diodes when the voltage has not reached the depletion voltage. In addition, the VBias has not a "natural" way to be included in our analysis. When we are talking about these limitations we are not referring to the constrictions that the theorems and methods have, but have to be considered anyway.

Chapter 5

Conclusions.

Although this alternative way of simulating the transitory currents has its own limitations, the resulting fields that have been computed by the relaxational and charge distribution methods fits with the previous models for similar detectors. The resulting values of the depletion voltage of $V_{dep}^A = 0.91$ V and $V_{dep}^B = 1.32$ V are consistent too. It is difficult to compare with other studies because this pixel configuration was not studied before. The characterization of the signals' profile has been a success, were a charge recovery above the 99.5% has been achieved. Transient currents show clearly the main features of the signal induction and their relation with the charge type and the geometry of the detectors. It was also possible to obtain bipolar signal induction from the first pixel neighbours. Magnetic field affects the tendency of the charge's path above values of $B = 10^3$ T, far away of the real experimental values used on CMS. The dependence with the B direction was also characterized. These final results predict that the magnetic fields that CERN's particle accelerators can reach are not enough to show charge sharing.

This project has provided a very useful tool for the characterization of complex sensor architectures, and it has been applied in a preliminary study of the influence of magnetic fields on charge sharing. The project is still under development, as data should support, as it seems to be indicating, and validate the results of the simulations, as well as a deeper analysis of systematic uncertainties sources should be pursued. It is planned to compare experimental I-V and C-V curves of 3D pixels to validate the predicted depletion voltages, and use techniques such as those based on two-photon absorption (TPA) to study the transient signal and directly compared with our simulation results. However, the preliminary comparative we have performed in this work already shown consistent results with more sophisticated simulation tools and experimental data.

Bibliography

- [1] R.F.H. Hunter. *Development and evaluation of novel, large area, radiation hard silicon microstrip sensors for the atlas ITk experiment at the HL-LHC*. PhD thesis, 08 2017.
- [2] About cms. [<https://cms.cern/detector>].
- [3] Ulrich Husemann – University of Glasgow. A new pixel detector for the cms experiment. [[http : //ekpwww.etp.kit.edu/husemann/talks/husemann_cms_pixel_heidelberg_20120508.pdf](http://ekpwww.etp.kit.edu/husemann/talks/husemann_cms_pixel_heidelberg_20120508.pdf)].
- [4] Markus Axer. Development of a test system for the quality assurance of silicon microstrip detectors for the inner tracking system of the cms experiment /. 02 2022.
- [5] Ix-B G. Ferreira, J. G. Herrera, and L. Villaseñor. The drift chambers handbook, introductory laboratory course (based on, and adapted from, a h walenta’s course notes). *Journal of physics. Conference series*, 18(1):346–361, 2005.
- [6] KEK Detector technology project. Overview of research work: Soi (silicon-on-insulator). [[https : //rd.kek.jp/lab025e.html](https://rd.kek.jp/lab025e.html)].
- [7] J. Gillies. Luminosity? why don’t we just say collision rate? [[https : //home.cern/news/opinion/cern/luminosity – why – dont – we – just – say – collision – rate](https://home.cern/news/opinion/cern/luminosity-why-dont-we-just-say-collision-rate)].
- [8] E. Currás, J. Duarte-Campderrós, M. Fernández, A. García, G. Gómez, J. González, R. Jaramillo, D. Moya, I. Vila, S. Hidalgo, M. Manna, G. Pellegrini, D. Quirion, D. Pitzl, A. Ebrahimi, T. Rohe, and S. Wiederkehr. Study of small-cell 3d silicon pixel detectors for the high luminosity lhc. Technical Report spectrometers, Deutsches Elektronen-Synchrotron, DESY, Hamburg, 2019.
- [9] 3d — a proposed new architecture for solid-state radiation detectors. *Nuclear Instruments and Methods in Physics Research Section A: Accelerators, Spectrometers, Detectors and Associated Equipment*, 395(3):328–343, 1997. Proceedings of the Third International Workshop on Semiconductor Pixel Detectors for Particles and X-rays.
- [10] Gilberto Giugliarelli and on behalf of the ATLAS Collaboration. Modeling of radiation damage effects and digitization for 3d silicon pixel atlas detectors. *Nuclear instruments methods in physics research. Section A, Accelerators, spectrometers, detectors and associated equipment*, 924:208–213, 2019.
- [11] J. Duarte-Campderros, E. Currás, M. Fernández, G. Gómez, A. García, J. González, E. Silva, I. Vila, R. Jaramillo, M. Meschini, R. Ceccarelli, M. Dinardo, S. Gennai, L. Moroni, D. Zuolo, L. Demaria, E. Monteil, L. Gaioni, A. Messineo, G. F.

- Dalla Betta, R. Mendicino, M. Boscardin, S. Hidalgo, A. Merlos, G. Pellegrini, D. Quirion, M. Manna, and on behalf of the CMS Collaboration. Results on proton-irradiated 3d pixel sensors interconnected to rd53a readout asic. *Nuclear instruments methods in physics research. Section A, Accelerators, spectrometers, detectors and associated equipment*, 944:162625, 2019.
- [12] David Pennicard – University of Glasgow. Introduction to sentaurus tcad. [<https://slideplayer.com/slide/776407/>].
- [13] CERN collaboration. About garfield++. [[https : //gar fieldpp.web.cern.ch/gar fieldpp/about/](https://garfieldpp.web.cern.ch/garfieldpp/about/)].
- [14] CERN collaboration. Allpix squared. [[https : //project – allpix – squared.web.cern.ch/project – allpix – squared/](https://project-allpix-squared.web.cern.ch/project-allpix-squared/)].
- [15] J. Calvo, P. de Castro, A. D. González-Pardo, M. F. García, M. Moll, U. Senica, and I. Vila. Tracs: A multi-thread transient current simulator for micro strips and pad detectors. *Nuclear instruments methods in physics research. Section A, Accelerators, spectrometers, detectors and associated equipment*, 917:77–85, 2019.
- [16] William R. Leo. *Techniques for nuclear and particle physics experiments: a how-to approach*. Springer, New York;Berlin [etc.];, 2nd rev. edition, 1994.
- [17] D. Bortoletto. How and why silicon sensors are becoming more and more intelligent? *Journal of instrumentation*, 10(8):C08016–C08016, 2015.
- [18] L. Bryngemark and for t. A. Collaboration. Charged pion identification at high pt in alice using tpc de/dx. 2011.
- [19] Institute of Experimental and Applied Physics (Prague). Minimum ionizing particles @ONLINE.
- [20] Bart Bruyneel. Weighting potentials. [<https://ns.ph.liv.ac.uk/EGAN/files/tuesday/Bruyneel-EGAN-School-P1>].
- [21] Zhong He. Review of the shockley–ramo theorem and its application in semiconductor gamma-ray detectors. *Nuclear instruments methods in physics research. Section A, Accelerators, spectrometers, detectors and associated equipment*, 463(1):250–267, 2001.
- [22] Werner Riegler. An application of extensions of the ramo-shockley theorem to signals in silicon sensors. 2018.
- [23] Justin C. W. Song and Leonid S. Levitov. Shockley-ramo theorem and long-range photocurrent response in gapless materials. *Physical review. B, Condensed matter and materials physics*, 90(7), 2014;2011;.
- [24] David G. Robertson. Relaxation methods for partial differential equations: Applications to electrostatics. 2010.
- [25] The NumPy community. Numpy user guide - release 1.22.0. [[https : //numpy.org/doc/stable/numpy – user.pdf](https://numpy.org/doc/stable/numpy-user.pdf)].
- [26] The SciPy community. Scipy user guide. [[https : //scipy.github.io/devdocs/tutorial/index.html#user – guide](https://scipy.github.io/devdocs/tutorial/index.html#user-guide)].

- [27] David-Leon Pohl Bonn University. Weighting field of a 3d sensor. [[https :
//scarce.readthedocs.io/en/latest/Examples.html](https://scarce.readthedocs.io/en/latest/Examples.html)].
- [28] Clara Lasasosa García, Jorge Duarte Campderros, Alicia Calderón Tazón, and Universidad d. Cantabria. *Implementation of the 3D pixel sensor response into CMSSW: Implementación de la respuesta del sensor de píxeles 3D en CMSSW*. PhD thesis, 2020.
- [29] A. La Rosa, M. Boscardin, G. . D. Betta, G. Darbo, C. Gemme, H. Pernegger, C. Piemonte, M. Povoli, S. Ronchin, A. Zoboli, N. Zorzi, E. Bolle, M. Borri, C. Da Via, S. Dong, S. Fazio, P. Grenier, S. Grinstein, H. Gjersdal, P. Hansson, F. Huegging, P. Jackson, M. Kocian, F. Rivero, O. Rohne, H. Sandaker, K. Sjobak, T. Slavicek, W. Tsung, D. Tsybychev, N. Vermes, and C. Young. Preliminary results of 3d-ddtc pixel detectors for the atlas upgrade. 2009.

Appendix A

Extra figures

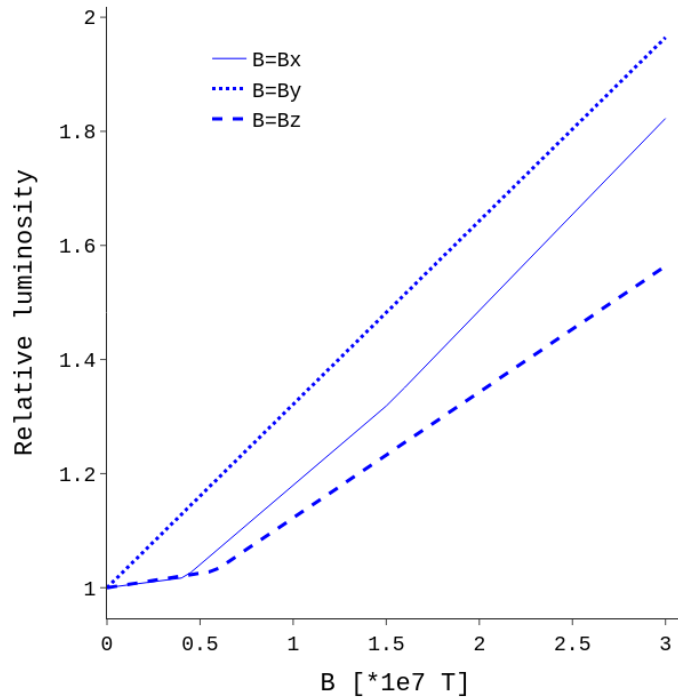


Figure A.1: Increment of the maximum response as function of the orientation and magnitude of the electric field ($25 \times 100 \times 150 \mu\text{m}^3$ pixel detector). Figure 4.21 shows the changes on the response map only for a given layer and normalized. This implies that the changes in absolute response are lost. This figure covers that gap by studying the increment on the normalized maximum signal from the case where no magnetic field is present.

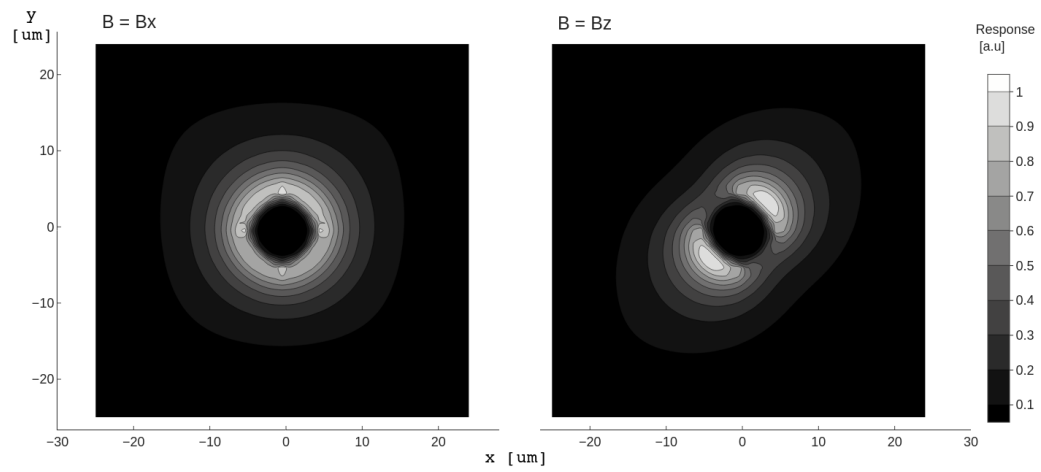


Figure A.2: Magnetic effects on the $50 \times 50 \times 150 \mu\text{m}^3$ pixel. The change in the behaviour of the response is present when high magnetic fields are applied.

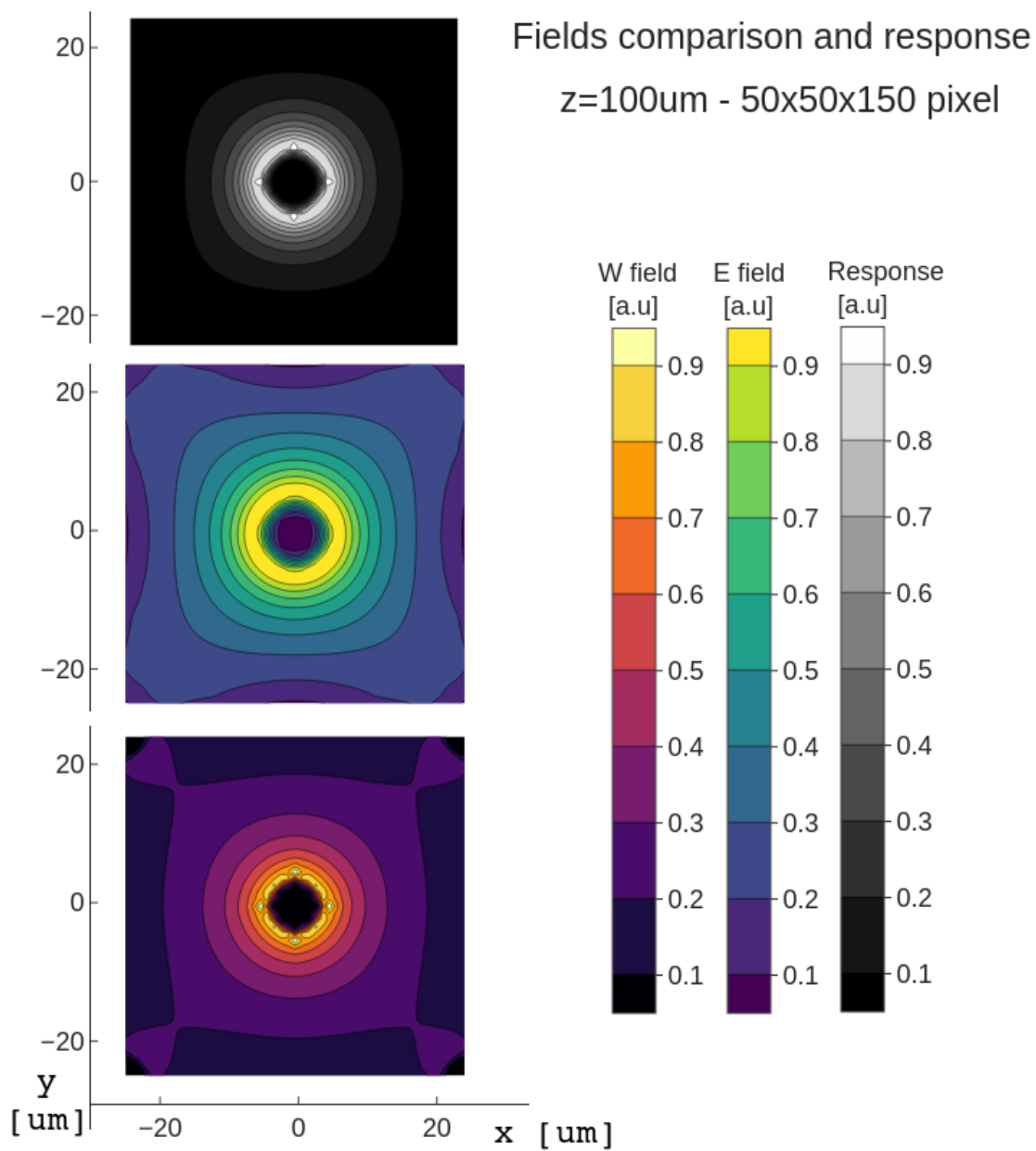


Figure A.3: Field comparison as it was shown in figure 4.11 for the $50 \times 50 \times 150 \mu\text{m}^3$ architecture. The difference between that two comparisons is clear.